Integrated Sensing and Communication for Symbiotic Radio Systems in Mobile Scenarios

Qin Tao, Xiaoling Hu, Shuowen Zhang, and Caijun Zhong, *Senior Member, IEEE*

***Abstract*— This paper presents a study on the integrated sensing and communication (ISAC) for symbiotic radio systems in mobile scenarios, where the receiver shared by the primary and secondary systems is capable of locating the moving object of secondary systems via estimating the direction of arrival (DoA), and detecting the symbols for both systems. For the considered symbiotic radio systems, the strong interference from the primary systems and moving object pose significant challenges for location sensing. Moreover, the symbol detection for symbiotic radio systems typically relies on channel state information (CSI), which would reduce the spectrum efficiency substantially. To address these challenges, this paper proposes a low-complexity and high-accuracy two-dimension DoA estimator based on the ratio of dual points on the main lobe using a single snapshot. The theoretical performance in terms of effective sensing probability and mean square error for the proposed estimator are provided in closed-form. To eliminate the dependence of symbol detection on CSI, we propose to fully capture the characteristic of the ISAC systems and introduce two types of DoA-assisted detectors to detect both the primary and secondary symbols. Specifically, the reciprocal linear detectors that use heuristic linear combiners and iterative detection to achieve mutual benefit for both transmissions, as well as a Manchester detector that can separate the primary and secondary signals, are proposed. Finally, the numerical results are provided to validate the correctness of the theoretical analysis, and demonstrate the superiority of the proposed DoA estimator and DoA-assisted detectors.**

***Index Terms*— Integration of sensing and communication, symbiotic radio, intelligent reflecting surface, DoA, symbol detection.**

Manuscript received 28 March 2023; revised 12 December 2023; accepted 5 March 2024. Date of publication 27 March 2024; date of current version 12 September 2024. The work of Qin Tao was supported in part by the National Natural Science Foundation of China under Grant 62301206 and in part by Zhejiang Provincial Natural Science Foundation of China under Grant LQ24F010005. The work of Xiaoling Hu was supported by the National Natural Science Foundation of China under Grant 62201084. The work of Shuowen Zhang was supported in part by the National Natural Science Foundation of China under Grant 62101474; and in part by the Research Grants Council, Hong Kong, SAR, China, under Grant 15230022. The associate editor coordinating the review of this article and approving it for publication was S. Ma. *(Corresponding author: Qin Tao.)*

Qin Tao is with the School of Information Science and Technology, Hangzhou Normal University, Hangzhou 311121, China (e-mail: taoqin@hznu.edu.cn).

Xiaoling Hu is with the State Key Laboratory of Networking and Switching Technology, Beijing University of Posts and Telecommunications, Beijing 100876, China (e-mail: xiaolinghu@bupt.edu.cn).

Shuowen Zhang is with the Department of Electronic and Information Engineering, The Hong Kong Polytechnic University, Hong Kong, China (e-mail: shuowen.zhang@polyu.edu.hk).

Caijun Zhong is with the College of Information Science and Electronic Engineering, Zhejiang University, Hangzhou 310027, China (e-mail: zhongcj0615@163.com).

Color versions of one or more figures in this article are available at https://doi.org/10.1109/TWC.2024.3379653.

Digital Object Identifier 10.1109/TWC.2024.3379653

I. Introduction

SYMBIOTIC radio technology is one of the promising solution for the future internet of things (IoT) networks [1], [2], [3], [4], which enables the passive IoT nodes of the secondary systems, such as tag and intelligent reflecting surface (IRS), modulates its information onto the radio frequency (RF) signal emitted by the primary systems, thereby significantly reducing the hardware and power cost of the systems. Additionally, the secondary systems can also provide rich multi-path gains to primary systems by reconfiguring the wireless channel environment [5], [6]. In this case, the symbiotic radio systems enables mutual benefits for the primary and secondary systems via cooperation.

However, the mutual interference between primary and secondary transmissions makes the signal detection for both systems challenging and various detectors have been proposed. For instance, the index modulation (IM) on the receive antenna was proposed for the secondary transmission [7], [8], and the cooperation between primary and secondary transmission was design to avoid mutual interference. Some works, such as [9] and [10], proposed to employ IM on IRS elements and use compressive sensing (CS) and matrix decomposition methods to detect primary and secondary information for single-user and multi-user scenarios. Meanwhile, the work [11] proposed to transfer the IRS binary symbol by selecting two reflection matrices that were designed to minimize the transmit power, and a pattern recognition strategy is proposed for symbol detection. Those detector all necessitate full channel state information (CSI), which could result in substantial spectrum wastage, particularly in the case with high-dimensional IRS [12]. In response to this, the work [13] introduced a data-driven semi-blind clustering receiver, employing an expectation-maximization algorithm based on Gaussian mixture models and a modulation-constrained expectation-maximization detection algorithm. However, this semi-blind receiver still relies on a limited number of pilot signals for parameter learning. Exploring new detection schemes without CSI is deemed worthwhile to enhance the system's spectrum efficiency.

Many IoT applications necessitate not only communication with IoT nodes, but also localization to enable functionalities such as cargo tracking, luggage retrieval, and smart home automation. For location sensing, the direction of arrival (DoA)-based approach is widely used due to its excellent noise resistance performance [14], including the time-domain, frequency domain, and compressive sensing (CS) methods.

Specifically, the time-domain methods, such as multiple signal classification (MUSIC) methods [15], estimation of signal parameters via rotational invariance techniques (ESPRIT) [16] and their variants, can achieve high accuracy, however, require *large number of signal snapshots in the same location*, which would cause significant sensing delay and is unsuitable for the mobile scenarios. The frequency-domain and CS methods can be done with single snapshot by exploiting the discrete Fourier transformation (DFT) spectrum or the sparsity of channels, however, the accuracy is greatly limited to the angle quantization [17] or dictionaries' resolution [18]. To tackle these difficulties, the off-grid CS methods were proposed to improve the DoA accuracy, but their complexity is rather high [19]. An angle correction method was proposed in [20] by using the Taylor expansion on the basis of DFT-search to find the bias between the quantized DoA and real DoA, however, it would suffer performance loss due to the first-order approximation.

Considering the scenario depicted in Fig. 1(a), where a passenger in the airport needs to maintain regular communication while simultaneously identify and locate the luggage attached with an IRS that *moves* along a belt. To enhance efficiency in simultaneous transmission and localization, this paper focuses on the design of integrated sensing and communication (ISAC) for symbiotic radio systems in mobile scenarios. The ISAC technique, a current focal point of research [21], [22], [23], [24], [25], [26], involves the coordinated use of sensing and communication spectrum and infrastructure within a unified system. However, all the existing works on ISAC exclusively concentrate on scenarios involving only the primary systems [27], [28], [29]. To the best of our knowledge, this is the first work to address ISAC for symbiotic radio systems.

For the considered ISAC symbiotic radio systems in mobile scenarios, the unknown-yet-strong interference from the primary systems and the moving object pose significant challenges for locating sensing, rendering the existing sensing methods unsuitable. Specifically, the time-domain methods are not applicable for mobile scenario since it requires numerous snapshots in a fixed location, and the accuracy of frequency-domain and CS methods are significantly affected by the interference and quantization resolution. Moreover, since the primary systems need to transmit informative signals to maintain its communication, indicating that no pilots can be emitted to estimate the CSI for the secondary systems, thereby making the symbol detections for symbiotic radio systems challenging. To tackle the aforementioned difficulties, in this paper, we propose a novel two-dimensional (2D) DoA estimator and DoA-assisted detectors. The main contributions are summarized as follows.

- First of all, we propose a 2D DoA estimator based on the Ratio of Dual Points on the Main Lobe (Ratio-DPML) to obtain the spatial location of a moving IRS, which requires only a single snapshot and a UPA receiver. This approach has low complexity but high accuracy, and can reduce hardware costs compared to configurations that use distributed reference devices. Then, the theoretical performance of the proposed DoA estimator is analyzed, including the effective sensing probability and mean squared error (MSE). By analyzing the close-form expressions, the valuable insights can be seen and can provide guidance for designing the ISAC for symbiotic radio systems.
- To eliminate the dependence of symbol detection on CSI, we introduce two types of DoA-assisted detectors to detect the primary and secondary symbols. Specifically, reciprocal linear detectors using heuristic linear combiners are investigated to achieve mutual benefit for primary and secondary transmissions by operating iterative detection. Moreover, to eliminate the addictive interference between primary and secondary transmissions, we propose a Manchester-coding based detector to separate the primary and secondary signals, thereby significantly improving the detection performance.
- Finally, the numerical results are provided to evaluate the performance of the proposed Ratio-DPML based DoA estimator and DoA-assisted detectors, as well as validate the theoretical analysis. Besides, we also compare the proposed DoA estimator and DoA-assisted detectors with several benchmarks to illustrate the superiority of the proposed methods.

The remainder of the paper is organized as follows. Section II provides a description of the system model. Section III proposes the Ratio-DPML based DoA estimator and analyzes its theoretical performance. Section IV studies the DoA-assisted detectors for symbiotic radio systems. Section VI presents the numerical results and discussions. Finally, Section VII concludes the paper.

Notations: Scalars are denoted by lowercase letters, while vectors and matrices are denoted by boldfaced letters. We use $|z|$ to denote the absolute value of a complex number z, respectively. The Hermitian, p-norm, and transpose of a matrix $\mathbf{A}$ are denoted by $\mathbf{A}^H$, $\|\mathbf{A}\|_p$, and $\mathbf{A}^T$, respectively. The maximum value of vector $\mathbf{a}$ is represented by $\max(\mathbf{a})$. $\mathbf{I}_K$ denotes the identity matrix of size K. $\Re\{z\}$ denotes the real part of z. $\mathcal{CN}(\boldsymbol{\mu}, \boldsymbol{\sigma}^2)$ denotes the complex Gaussian distribution with mean $\boldsymbol{\mu}$ and variance $\boldsymbol{\sigma}^2$. $\mathbb{E}[z]$ and $\mathbb{D}[z]$ stand for the expectation and variance of a random variable z, respectively. $\mathbb{C}^{N\times M}$ and $\mathbb{N}$ represents an $N\times M$ complex matrix and integer set, respectively. The probability of event a is represented by $\Pr[a]$, while the probability density function (PDF) of variable z is denoted by $f_z(x)$. $\operatorname{sgn}(t) = 1$ if $t \geq 0$ while $\operatorname{sgn}(t) = -1$ if $t < 0$.

II. System Model

A. The Considered Scenario and Transmission Protocol

This paper considers the downlink transmission for a multiple-input multiple-output (MIMO) ISAC-symbiotic radio systems, as shown in Fig. 1(a). In this setup, the receiver, equipped with a $K_x \times K_y$ uniform planar array (UPA), communicates with the base station (BS) using a $M_x \times M_y$ UPA for primary transmission, while simultaneously identifies and locates the moving luggage/cargo through secondary transmission.[1] Without loss of generality, we assume that the location of BS and receiver are fixed and denoted as $(0, 0, 0)$ and (a, b, c), respectively, and the luggage moves along a belt on a constant vertical height with location (x, y, r), where r is known a prior. As such, the spatial location of luggage can be determined by obtaining unknown x and y. To enable the luggage identification and positioning, an IRS with a $N_x \times N_y$ UPA is attached on its surface,[2] which can reflect the signal emitted by the BS and transmit its own information to the receiver through reflective modulation. In addition, it is crucial to note that the direction of the IRS beaming can be adjusted over a broad range of angles by changing the reflecting coefficients, ensuring effective secondary transmission provided that the receiver remains within the IRS's feasible beaming range. This can be achieved by intentionally and properly placing the pose of the IRS. This setting enables efficient sensing and communication through deep integration of primary and secondary systems, holding great potential for various applications, such as transportation industry, logistics management, smart cities, health care, and more.

Considering the stationary nature of the BS and receiver, we model the channel for BS-receiver link as quasi-static. This implies that the channel from the BS to the receiver remains unchanged during the coherence interval but changes independently between different coherence periods. However, recognizing the mobility of the IRS, we treat the channels between the BS-IRS and IRS-receiver as dynamically changing. We then provide the transmission protocol for the considered systems during each coherence time, as shown in Fig. 1(b). Specifically, at the beginning, the primary systems use the pilots and employs traditional channel estimation techniques to estimate the CSI for primary systems, while the secondary systems remains inactive. Following this, the primary systems begins information transmissions continuously, and the secondary systems provide both location and communication information to the receiver as required. In the ensuing sections, we aim to propose efficient methods to timely and accurately locate the moving luggage/IRS and detect the symbols for both primary and secondary transmissions.[3]

B. The Channel and Signal Model

Considering the millimeter wave scenarios, it is reasonable to assume that the scattered signals can be ignored due to their large-scale fading and line-of-sight path dominates, especially when leveraging the beamforming and combining gain inherent in a MIMO systems [25], [26], [30]. Denoting

[1]We take the example of single luggage in this paper to facilitate the analysis of the theoretical metrics of the systems, which can guide the design of ISAC systems.

[2]The IRS has compact dimensions and low power requirements, rendering it portable and easily attachable to luggage. For instance, in the context of a mmWave frequency band at $f = 27$ GHz, a 20×56 IRS occupies an area of approximately 0.056×0.078 m^2 and consumes power at a level of a few milliwatts [42].

[3]Note that as the luggage constantly moves along the belt, the strategy of BS estimating the luggage's location and subsequently relaying this information to the receiver would introduce significant delays.

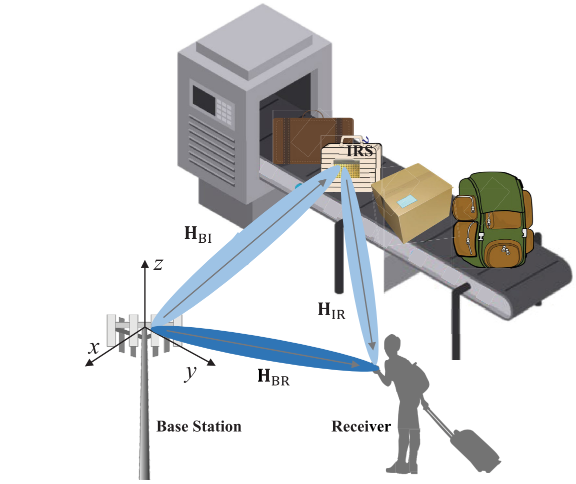

(a) The MIMO ISAC-symbiotic radio systems.

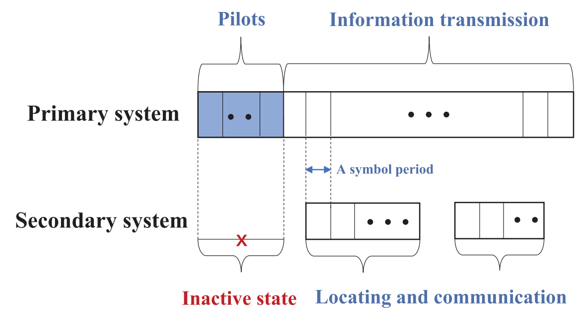

(b) The transmission protocol during one coherence interval.

Fig. 1. System model.

the channels from the BS to the IRS, from the IRS to the receiver, and from the BS to the receiver as $\mathbf{H}_{\mathrm{BI}}$, $\mathbf{H}_{\mathrm{IR}}$ and $\mathbf{H}_{\mathrm{BR}}$, respectively, they can be expressed as

$$\mathbf{H}_{\mathrm{BI}} = \alpha_{\mathrm{BI}} \mathbf{a}_{N_x \times N_y}\left(\vartheta_{\mathrm{IB},x}, \vartheta_{\mathrm{IB},y}\right) \mathbf{a}^H_{M_x \times M_y}\left(\vartheta_{\mathrm{BI},x}, \vartheta_{\mathrm{BI},y}\right), \quad (1)$$

$$\mathbf{H}_{\mathrm{IR}} = \alpha_{\mathrm{IR}} \mathbf{a}_{K_x \times K_y}\left(\vartheta_{\mathrm{RI},x}, \vartheta_{\mathrm{RI},y}\right) \mathbf{a}^H_{N_x \times N_y}\left(\vartheta_{\mathrm{RI},x}, \vartheta_{\mathrm{RI},y}\right), \quad (2)$$

$$\mathbf{H}_{\mathrm{BR}} = \alpha_{\mathrm{BR}} \mathbf{a}_{K_x \times K_y}\left(\vartheta_{\mathrm{RB},x}, \vartheta_{\mathrm{RB},y}\right) \mathbf{a}^H_{M_x \times M_y}\left(\vartheta_{\mathrm{BR},x}, \vartheta_{\mathrm{BR},y}\right), \quad (3)$$

respectively. Here α_τ represents the corresponding channel complex gain; $\mathbf{a}_{p_x \times p_y}\left(\vartheta_x, \vartheta_y\right) = \mathbf{a}_{p_x}\left(\vartheta_x\right) \otimes \mathbf{a}_{p_y}\left(\vartheta_y\right)$ with steering vector $\mathbf{a}_p\left(\vartheta\right) = [1, e^{j2\pi\frac{d}{\lambda}\vartheta}, \cdots, e^{j2\pi\frac{d}{\lambda}(p-1)\vartheta}]^T$ and $\otimes$ represents the Kronecker product; d denotes the distance between two adjacent antennas [25]; $\vartheta_{\tau,x}$ and $\vartheta_{\tau,y}$ are the corresponding effective angles of departure/arrival along x and y axis, respectively, which can be calculated via the location of the devices [26]. We take $\vartheta_{\mathrm{RI},x}$ and $\vartheta_{\mathrm{RI},y}$ for example, which can be calculated via

$$\vartheta_{\mathrm{RI},x} = \frac{a - x}{d_{\mathrm{RI}}}, \quad \vartheta_{\mathrm{RI},y} = \frac{b - y}{d_{\mathrm{RI}}}, \quad (4)$$

where $d_{\mathrm{RI}} = \sqrt{(x-a)^2 + (y-b)^2 + (r-c)^2}$. Based on Eq. (4), we see that the unknown location x and y can be obtained by estimating the 2D DoA $\vartheta_{\mathrm{RI},x}$ and $\vartheta_{\mathrm{RI},y}$.

For the downlink transmission, the receiver can hear both the direct signal from the BS and the reflected signal from the IRS. The receiving signal can be mathematically represented as

$$\mathbf{y}_{\mathrm{R}}=\sqrt{P_s}\mathbf{H}_{\mathrm{BR}}\mathbf{w}\mathrm{s}_{\mathrm{B}}+\sqrt{P_s}\mathbf{H}_{\mathrm{IR}}\mathrm{diag}(\boldsymbol{\theta})\mathbf{H}_{\mathrm{BI}}\mathbf{w}\mathrm{s}_{\mathrm{B}}\mathrm{s}_{\mathrm{I}}e^{-j2\pi\mathrm{v}_{\mathrm{R}}t}+\mathbf{n}_{\mathrm{R}}, \tag{5}$$

where s_{B} is the primary/BS information and assumed to adopt binary phase shift keying (BPSK) modulation for the ease of exposition, i.e., $\mathrm{s}_{\mathrm{B}} = \pm 1$; s_{I} represents the secondary/IRS information satisfying $\mathbb{E}[|\mathrm{s}_{\mathrm{I}}|^2] = 1$, whose symbol period is equals to s_{B} and modulation strategy will be elaborated in Section IV; $\boldsymbol{\theta} \in \mathbb{C}^{N_x N_y \times 1}$ denotes the reflecting vector of the IRS; $\sqrt{P_s}$ represents the power of BS; $\mathbf{n}_{\mathrm{R}} \sim \mathcal{CN}(0, \sigma^2 \mathbf{I}_{K_x K_y})$ is the noise at the receiver; v_{R} represents the doppler frequency shift; Importantly, $\mathbf{w}$ is the beamforming vector of the BS, and the rank-1 channels allow the combining of the transmit beam $\mathbf{w}$ with the departure steering vectors, rendering the MIMO case analogous to the single-input multiple-output case. Specifically, for simplicity in notation, we denote $G_P = \mathbf{a}^H_{M_x \times M_y}(\vartheta_{\mathrm{BR},x}, \vartheta_{\mathrm{BR},y})\mathbf{w}$ and $G_S = \mathbf{a}^H_{M_x \times M_y}(\vartheta_{\mathrm{BI},x}, \vartheta_{\mathrm{BI},y})\mathbf{w}$ as the beamforming gains of the primary and secondary systems, respectively.[4] The remaining equivalent channels for the BS-IRS and BS-receiver links are denoted as $\mathbf{h}_{\mathrm{BI}} = \alpha_{\mathrm{BI}}\mathbf{a}_{N_x \times N_y}(\vartheta_{\mathrm{IB},x}, \vartheta_{\mathrm{IB},y})$, $\mathbf{h}_{\mathrm{BR}} = \alpha_{\mathrm{BR}}\mathbf{a}_{K_x \times K_y}(\vartheta_{\mathrm{RB},x}, \vartheta_{\mathrm{RB},y})$, respectively. Consequently, Eq. (5) can be simplified as

$$\begin{aligned}\mathbf{y}_{\mathrm{R}} = \sqrt{P_s}\mathbf{h}_{\mathrm{BR}}\mathrm{s}_{\mathrm{B}}G_P + \sqrt{P_s}\mathbf{H}_{\mathrm{IR}}\mathrm{diag}(\boldsymbol{\theta})\\ \times \mathbf{h}_{\mathrm{BI}}\mathrm{s}_{\mathrm{B}}\mathrm{s}_{\mathrm{I}}G_S e^{-j2\pi\mathrm{v}_{\mathrm{R}}t} + s\mathbf{n}_{\mathrm{R}}.\end{aligned} \tag{6}$$

Then, the receiver leverages $\mathbf{y}_{\mathrm{R}}$ to locate the luggage/IRS, as well as detects both primary and secondary information. It is worth noting that for the considered symbiotic radio systems, the tasks of location sensing and symbol detection are particularly challenging: First of all, the interference from the primary systems and mobile scenario render the existing sensing methods unsuitable; Secondly, since the primary systems should maintain its information transmission during the active time of secondary systems, there are no pilots available for estimating the secondary system's CSI, making it difficult to detect the mixed primary and secondary signals without CSI. To address these issues, we propose a novel 2D DoA estimator that enables efficient and accurate location sensing for moving objects in Section III, and useful DoA-assisted detectors in Section IV.

III. The 2D DoA Estimator Based on Ratio-DPML

The time-domain DoA estimation methods, such as MUSIC and ESPRIT, as well as their derivative methods, typically require a significant number of samples for estimating the signal and noise subspace, resulting in high overhead and making them unsuitable for mobile scenarios. Additionally, the existing frequency-domain and CS methods suffer great performance loss due to the interference and limited quantization resolution, also, the computational cost is extremely high, especially for the 2D case. In light of this, we propose a low-complexity and high-accuracy 2D DoA estimator based on a single snapshot, and analyze its theoretical performance to provide guidance for system design.

A. The Ratio-DPML Based 2D DoA Estimator

We first construct the 2D DFT spectrum, or known as discrete beam pattern diagram, using a single snapshot $\mathbf{y}_{\mathrm{R}}$ as

$$\mathbf{Z} = \mathrm{Abs}(\mathbf{W}\mathbf{Y}_{\mathrm{R}}) \in \mathbb{C}^{K_x \times K_y}, \tag{7}$$

where $\mathrm{Abs}(\mathbf{X})$ returns the absolute value of each element in array $\mathbf{X}$; $\mathbf{Y}_{\mathrm{R}}$ is a diagonal expansion version of $\mathbf{y}_{\mathrm{R}}$ and can be written as $\mathbf{Y}_{\mathrm{R}} = \mathrm{diag}(\underbrace{\mathbf{y}_{\mathrm{R}}, \mathbf{y}_{\mathrm{R}}, \ldots \mathbf{y}_{\mathrm{R}}}_{K_y})$; $\mathbf{W} \in \mathbb{C}^{K_x \times K_x K_y^2}$ is a 2D DFT matrix, whose elements can be expressed as

$$\begin{aligned}&[\mathbf{W}]_{i,(j-1)K_xK_y+1:jK_xK_y}\\ &= \frac{1}{K_xK_y}\mathbf{a}^H_{K_x \times K_y}\left(\vartheta_{\mathrm{BR},x} + \frac{2(i-1)}{K_x}, \vartheta_{\mathrm{BR},y} + \frac{2(j-1)}{K_y}\right),\end{aligned} \tag{8}$$

where $i = 1, \ldots K_x$, $j = 1, \ldots K_y$. As previously illustrated, the channel for the primary systems $\mathbf{h}_{\mathrm{BR}}$ is known a prior via traditional channel estimation method, hence $\vartheta_{\mathrm{BR},x}$ and $\vartheta_{\mathrm{BR},y}$ are known a prior.[5] It is worth noting that the first element of $\mathbf{W}\mathbf{Y}_{\mathrm{R}}$, i.e., $[\mathbf{W}\mathbf{Y}_{\mathrm{R}}]_{1,1}$, still contains the direct link interference $K_xK_y|\alpha_{\mathrm{BR}}|\sqrt{P_s}\mathrm{s}_{\mathrm{B}}$, where s_{B} is unknown. Observing the fact that the equivalent path gain for the direct link is much larger than that of the cascaded link in $[\mathbf{W}\mathbf{Y}_{\mathrm{R}}]_{1,1}$, hence, the direct link interference can be removed by setting the first element of $\mathbf{Z}$ as

$$\begin{aligned}Z_{1,1} = \min\Big\{&\left|[\mathbf{W}\mathbf{Y}_{\mathrm{R}}]_{1,1} - K_xK_y|\alpha_{\mathrm{BR}}|\sqrt{P_s}\right|,\\ &\left|[\mathbf{W}\mathbf{Y}_{\mathrm{R}}]_{1,1} + K_xK_y|\alpha_{\mathrm{BR}}|\sqrt{P_s}\right|\Big\}.\end{aligned} \tag{9}$$

To better understand the 2D DFT spectrum $\mathbf{Z}$, using the relationship $(\mathbf{U}\otimes\mathbf{V})(\mathbf{P}\otimes\mathbf{Q}) = (\mathbf{UP})\otimes(\mathbf{VQ})$, where $\mathbf{U} \in \mathbb{C}^{m\times n}$, $\mathbf{V} \in \mathbb{C}^{s\times t}$, $\mathbf{P} \in \mathbb{C}^{n\times p}$ and $\mathbf{Q} \in \mathbb{C}^{t\times q}$, the i-th column and j-th row of $\mathbf{Z}$ can be calculated as

$$\begin{aligned}Z_{i,j} = \Bigg|&\sqrt{P_s}\alpha_{\mathrm{cas}}\mathrm{s}_{\mathrm{B}}\mathrm{s}_{\mathrm{I}}\left[\mathbf{a}^H_{K_x}\left(\vartheta_{\mathrm{BR},x} + \frac{2(i-1)}{K_x}\right)\mathbf{a}_{K_x}(\vartheta_{\mathrm{RI},x})\right]\\ &\times\left[\mathbf{a}^H_{K_y}\left(\vartheta_{\mathrm{BR},y} + \frac{2(j-1)}{K_y}\right)\mathbf{a}_{K_y}(\vartheta_{\mathrm{RI},y})\right] + n_{i,j}\Bigg|,\end{aligned} \tag{10}$$

where $\alpha_{\mathrm{cas}} = G_S\alpha_{\mathrm{IR}}e^{-j2\pi\mathrm{v}_{\mathrm{R}}t}\mathbf{a}^H_{N_x\times N_y}(\vartheta_{\mathrm{RI},x}, \vartheta_{\mathrm{RI},y})\,\mathrm{diag}(\boldsymbol{\theta})\,\mathbf{h}_{\mathrm{BI}}$. It is obvious that $|\alpha_{\mathrm{cas}}|$ can be maximized by letting $\boldsymbol{\theta}^* = \mathbf{a}_{N_x\times N_y}(-\vartheta_{\mathrm{IB},x} + \vartheta_{\mathrm{RI},x}, -\vartheta_{\mathrm{IB},y} + \vartheta_{\mathrm{RI},x})$, and the resulting object value can be obtained as $|\alpha_{\mathrm{cas}}| = |G_S\alpha_{\mathrm{IR}}\alpha_{\mathrm{BI}}|N_xN_y$;

[4]In the realm of MIMO ISAC-symbiotic radio systems, where power budgets are constrained, achieving a delicate equilibrium in the performance of both primary and secondary systems is paramount. This equilibrium is intricately tied to the thoughtful design of the BS beamforming vector $\mathbf{w}$. It is important to note that the design of $\mathbf{w}$ is contingent upon specific system requirements, a topic that surpasses the current scope of this paper. However, we recognize its significance and earmark it as a focal point for our future research efforts.

[5]Note that the ensuing analysis remains applicable even in scenarios with channel estimation errors by treating the residual interference from primary systems as noise, albeit with some performance loss.

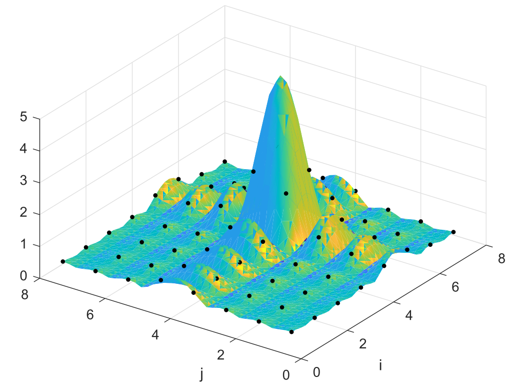

(a) The front view of $\mathbf{z}$.

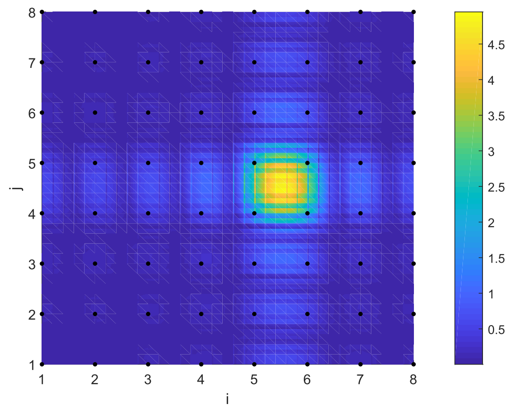

(b) The top view of $\mathbf{z}$.

Fig. 2. The 2D DFT spectrum.

$n_{i,j} = \frac{1}{K_x K_y}\mathbf{a}^H_{K_x\times K_y}\left(\vartheta_{\mathrm{BR},x}+\frac{2(i-1)}{K_x},\vartheta_{\mathrm{BR},y}+\frac{2(j-1)}{K_y}\right)\mathbf{n}_R$ follows $n_{i,j} \sim \mathcal{CN}(0,\sigma^2)$ and is independent of arbitrary $n_{i',j'}$ when $i \neq i'$ and $j \neq j'$. Denoting $\mathbf{u} = [u_1,\dots u_{K_x}]^T$ with $u_i = \frac{1}{K_x}\mathbf{a}^H_{K_x}\left(\vartheta_{\mathrm{BR},x}+\frac{2(i-1)}{K_x}\right)\mathbf{a}_{K_x}\left(\vartheta_{\mathrm{RI},x}\right)$ and $\mathbf{v} = [v_1,\dots v_{K_x}]^T$ with $v_j = \frac{1}{K_y}\mathbf{a}^H_{K_y}\left(\vartheta_{\mathrm{BR},y}+\frac{2(j-1)}{K_y}\right)\mathbf{a}_{K_y}\left(\vartheta_{\mathrm{RI},y}\right)$, the 2D DFT spectrum without noise can be expressed as

$$\mathbf{z} = \sqrt{P_s}\left|\alpha_{\mathrm{cas}}s_{\mathrm{B}}s_{\mathrm{I}}\mathbf{u}\mathbf{v}^T\right| \tag{11}$$

with $z_{i,j} = \sqrt{P_s}\left|\alpha_{\mathrm{cas}}s_{\mathrm{B}}s_{\mathrm{I}}u_i v_j\right|$. The front and top views of $\mathbf{z}$ are plotted in Fig. 4 for the purpose of intuitive understanding. Based on Eq. (11), we find that the rows of $\mathbf{z}$ can be regarded as the DFT spectrum for $\mathbf{a}_{K_y}(\vartheta_{\mathrm{RI},y})$ with varied amplitudes, while the columns of $\mathbf{z}$ can be regarded as the DFT spectrum for $\mathbf{a}_{K_x}(\vartheta_{\mathrm{RI},x})$ with varied amplitudes. Hence, we can use the columns and rows of $\mathbf{z}$ to estimate $\vartheta_{\mathrm{RI},x}$ and $\vartheta_{\mathrm{RI},y}$ independently in similar way. Moreover, for each column or row, there are two points on the main lobe and one point on the side lobe, and they follow the relationship:

Lemma 1: For the ideal case without noise, the largest two values of arbitrary column or row of $\mathbf{z}$ are always on the main lobe, and they are on either side of the peak of the continues DFT spectrum.

Proof: See Appendix A. ∎

We take the estimation of $\vartheta_{\mathrm{RI},x}$ for example with the help of *Lemma 1*. Denote $(i_1,j_1) = \arg\max_{i=1,\dots K_x, j=1,\dots K_y} z_{i,j}$ with the maximum value z_{i_1,j_1} and the equivalent angle on the DFT spectrum as $\theta_{1,x} = \vartheta_{\mathrm{BR},x}+\frac{2(i_1-1)}{K_x}-\vartheta_{\mathrm{RI},x}$. The largest value adjacent to z_{i_1,j_1} in the j_1 column is denoted as $z_{i_2,j_1} = \max(z_{i_1-1,j_1}, z_{i_1+1,j_1})$, where $i_2 = i_1-1$ when $z_{i_1-1,j_1} > z_{i_1+1,j_1}$, otherwise $i_2 = i_1+1$, and the corresponding equivalent angle is denoted as $\theta_{2,x} = \vartheta_{\mathrm{BR},x}+\frac{2(i_2-1)}{K_x}-\vartheta_{\mathrm{RI},x}$.[6] According to the formula of summation for geometric sequence, z_{i_1,j_1} reaches the peak of continues DFT spectrum when $\vartheta_{\mathrm{BR},x}+\frac{2(i_1-1)}{K_x}-\vartheta_{\mathrm{RI},x} = 0$, however, we can not always achieve this goal due to the limited samples and integer constraint on i [17]. Based on the relationship of z_{i_1,j_1} and z_{i_2,j_1} proposed in *Lemma 1*, we see that the true value of $\vartheta_{\mathrm{RI},x}$ is always between $\vartheta_{\mathrm{BR},x}+\frac{2(i_1-1)}{K_x}$ and $\vartheta_{\mathrm{BR},x}+\frac{2(i_2-1)}{K_x}$. Though the work [20] proposed to use the Taylor expansion to estimate the bias from $\vartheta_{\mathrm{BR},x}+\frac{2(i_1-1)}{K_x}$, however, it definitely suffers some performance loss with first-order approximations and the computational complexity is high by processing matrix inversion operation. In this paper, we propose to utilize the ratio of z_{i_1,j_1} and z_{i_2,j_1} to estimate $\vartheta_{\mathrm{RI},x}$ with high accuracy and low complexity.

Theorem 1: For the ideal case without noise, by using the ratio of z_{i_1,j_1} and z_{i_2,j_1}, the value of $\vartheta_{\mathrm{IR},x}$ can be obtained as

$$\vartheta_{\mathrm{RI},x} = \vartheta_{\mathrm{BR},x}+\frac{2(i_1-1)}{K_x}+\frac{2\phi_x}{\pi}-2k_x, \tag{12}$$

where $\phi_x = \arctan\left(\frac{\Delta_x z_{i_2,j_1}\sin\frac{\pi}{K_x}}{z_{i_1,j_1}+z_{i_2,j_1}\cos\frac{\pi}{K_x}}\right)$, $\Delta_x = \mathrm{sgn}(\theta_{1,x}-\theta_{2,x})$ and k_x is an integer satisfying $k_x \in (-\frac{1}{2K_x}+\frac{\phi_x}{\pi},\frac{\phi_x}{\pi})$.

Proof: See Appendix B. ∎

Theorem 1 provides an efficient approach to estimate $\vartheta_{\mathrm{RI},x}$ by exploiting the ratio of dual point on the main lobe, named as Ratio-DPML based DoA estimator, which offers real-time tracking of a moving target using single snapshot. Moreover, the use of a UPA receiver enables 2D spatial location with a single receiving device, making it a cost-effective alternative to the configurations that require distributed reference devices like multi-BS [31], [32] or multi-IRS [25]. For the practical scenario with noise, the proposed estimator can also be used, the process is summarized in **Algorithm 1**. Firstly, the 2D DFT spectrum $\mathbf{Z}$ is constructed without direct link interference. Then the maximum value of $\mathbf{Z}$ is then identified and denoted as Z_{I_1,J_1}, with the corresponding indices I_1 and J_1. After obtaining $Z_{I_2,J_1} = \max(Z_{I_1-1,J_1}, Z_{I_1+1,J_1})$ and $Z_{I_1,J_2} = \max(Z_{I_1,J_1-1}, Z_{I_1,J_1+1})$, the estimations for $\widehat{\vartheta_{\mathrm{RI},x}}$ and $\widehat{\vartheta_{\mathrm{RI},y}}$ can be computed as follows:

$$\widehat{\vartheta_{\mathrm{RI},x}} = \vartheta_{\mathrm{BR},x}+\frac{2(I_1-1)}{K_x}+\frac{2\phi'_x}{\pi}-2k_x$$
$$\text{and}\quad \widehat{\vartheta_{\mathrm{RI},y}} = \vartheta_{\mathrm{BR},y}+\frac{2(J_1-1)}{K_y}+\frac{2\phi'_y}{\pi}-2k_y, \tag{13}$$

[6]Note that since the DFT spectrum is periodic with 1, when $i_1 = 1$, we have $i_1-1 = K_x-1$; when $i_1 = K_x$, we have $i_1+1 = 1$.

where $\phi'_x = \arctan\left(\frac{\Delta_x Z_{I_2,J_1}\sin\frac{\pi}{2K_x}}{Z_{I_1,J_1}+Z_{I_2,J_1}\cos\frac{\pi}{2K_x}}\right)$ and $\phi'_y = \arctan\left(\frac{\Delta_y Z_{I_1,J_2}\sin\frac{\pi}{2K_y}}{Z_{I_1,J_1}+Z_{I_1,J_2}\cos\frac{\pi}{2K_y}}\right)$.

Algorithm 1 Algorithm 1 The Proposed Ratio-DPML Based DoA Estimator

Require: The receiving signal $\mathbf{y}_{\mathrm{R}}$ and BS-receiver channel $\mathbf{h}_{\mathrm{BR}}$.

Ensure: The estimated angles $\widehat{\vartheta_{\mathrm{RI},x}}$ and $\widehat{\vartheta_{\mathrm{RI},y}}$.

1: Construct $\mathbf{Z}$ using Eq. (7) and (9).

2: Find the largest value of $\mathbf{Z}$, denoted as Z_{I_1,J_1} and return the index I_1 and J_1.

3: Let $Z_{I_2,J_1} = \max(Z_{I_1-1,J_1}, Z_{I_1+1,J_1})$ and $z_{I_1,J_2} = \max(Z_{I_1,J_1-1}, Z_{I_1,J_1+1})$.

4: Compute $\widehat{\vartheta_{\mathrm{RI},x}}$ and $\widehat{\vartheta_{\mathrm{RI},y}}$ using Eq. (13).

It is evident that the accuracy of DoA estimation would be affected by the noise. In next subsection, we will analyze the theoretical performance of the proposed estimator, including the effective sensing probability and MSE.

B. The Probability of Effective Sensing

The first step of DoA estimation is finding the correct values of Z_{I_1,J_1}, Z_{I_2,J_1} and Z_{I_1,J_2}, indicating that the location of the largest three values of $\mathbf{Z}$ and $\mathbf{z}$ overlap, i.e., $I_1 = i_1$, $J_1 = j_1$, $I_2 = i_2$ and $J_2 = j_2$. In this case, we can ensure that the absolute value of error is within $\frac{1}{K_x}$ or $\frac{1}{K_y}$, and the resulting beam strength exceeds the half-wave amplitude since $\frac{1}{K_x\sin(\frac{\pi}{2K_x})} = \frac{2}{\pi} > 0.5$, we refer to this condition as effective sensing.

Strictly speaking, the probability of finding correct Z_{I_1,J_1}, Z_{I_2,J_1} and Z_{I_1,J_2} can be expressed as

$$\mathrm{P_{eff}} = \Pr\Big[(Z_{i_1,j_1} \geq \max_{i,j} Z_{i,j}) \cap (Z_{i_2,j_1} \geq Z_{i_3,j_1}) \cap (Z_{i_1,j_2} \geq Z_{i_1,j_3})\Big], \tag{14}$$

where i_3 and j_3 are the index of the side lobe point nearest to z_{i_1,j_1}. Since the event $Z_{i_1,j_1} \geq \max_{i,j} Z_{i,j}$ is correlated with both $Z_{i_2,j_1} \geq Z_{i_3,j_1}$ and $Z_{i_1,j_2} \geq Z_{i_1,j_3}$, the exact distribution of Eq. (14) is extremely hard to obtain. To address this issue, we resort to the asymptotic region. Denote the transmit signal-to-noise-ratio (SNR) as $\gamma = \frac{P_s}{\sigma^2}$. When either γ, K_xK_y, or N is large, the main power is concentrate on the main lobe and we have $\Pr[Z_{i_1,j_1} \geq \max_{i,j} Z_{i,j}] = 1$ with high probability. In this case, the closed-form of Eq. (14) can be obtained in Theorem 2.

Theorem 2: In the high γ, K_xK_y, or N regime, the probability of effective sensing can be approximated in closed-form as

$$\begin{aligned}
\mathrm{P}^{\infty}_{\mathrm{eff}} = &\frac{\Gamma(\alpha_{i_3,j_1}+\alpha_{i_2,j_1})}{\Gamma(\alpha_{i_3,j_1}+1)\Gamma(\alpha_{i_2,j_1})}\left(\frac{\beta_{i_3,j_1}}{\beta_{i_2,j_1}}\right)^{\alpha_{i_3,j_1}} \\
&\times \frac{\Gamma(\alpha_{i_1,j_3}+\alpha_{i_1,j_2})}{\Gamma(\alpha_{i_1,j_3}+1)\Gamma(\alpha_{i_1,j_2})}\left(\frac{\beta_{i_1,j_3}}{\beta_{i_1,j_2}}\right)^{\alpha_{i_1,j_3}} \\
&\times {}_2F_1\left(\alpha_{i_1,j_2}+\alpha_{i_1,j_3}, \alpha_{i_1,j_3}; \alpha_{i_1,j_3}+1; -\frac{\beta_{i_1,j_3}}{\beta_{i_1,j_2}}\right) \\
&\times {}_2F_1\left(\alpha_{i_2,j_1}+\alpha_{i_3,j_1}, \alpha_{i_3,j_1}; \alpha_{i_3,j_1}+1; -\frac{\beta_{i_3,j_1}}{\beta_{i_2,j_1}}\right),
\end{aligned}$$

where $\alpha_{i,j} = \frac{(p^2_{i,j}+\sigma^2)^2}{2p^2_{i,j}\sigma^2+\sigma^4}$ and $\beta_{i,j} = \frac{p^2_{i,j}+\sigma^2}{2p^2_{i,j}\sigma^2+\sigma^4}$ with $p_{i,j} = \sqrt{P_s}|\alpha_{\mathrm{cas}}u_iv_j|$; $\Gamma(x)$ denotes the Gamma function and ${}_2F_1(a,b;c;-x)$ denotes the hypergeometric function [33].

Proof: See Appendix C. ■

The closed-form expression $\mathrm{P}^{\infty}_{\mathrm{eff}}$ provides an efficient means for the evaluation of the effective sensing probability. However, it is still difficult to gain insights as it involves complicated hypergeometric and Gamma functions. Therefor, we resort to the numerical results to depicts the probability for effective sensing in Section V.

C. The Achievable MSE

Assuming the correct values of Z_{I_1,J_1}, Z_{I_2,J_1} and Z_{I_1,J_2} have been found, we then analyze the achievable MSE for the proposed estimator. As previously illustrated, $\vartheta_{\mathrm{RI},x}$ and $\vartheta_{\mathrm{RI},y}$ can be estimated independently, and the overall MSE for the systems can be regarded as the weighted sum of MSE_x and MSE_y, where MSE_x and MSE_y are the achievable MSE for estimating $\vartheta_{\mathrm{RI},x}$ and $\vartheta_{\mathrm{RI},y}$, respectively. The analysis for MSE_x and MSE_y are similar, and we present the derivation of MSE_x as an example.

Theorem 3: When $\theta_{1,x} \neq 0$, MSE_x can be accurately approximated as

$$\begin{aligned}
&\mathrm{MSE}_x \\
&\approx \frac{4\sin^4\phi_x}{\pi^2\sin^2\frac{\pi}{K_x}} \times \left[\frac{\alpha_{I_1,J_1}\beta_{I_2,J_1}}{(\alpha_{I_2,J_1}-1)\beta_{I_1,J_1}} + \left(\frac{p_{I_1,J_1}}{p_{I_2,J_1}}\right)^2\right. \\
&\quad \left. - 2\left(\frac{p_{I_1,J_1}}{p_{I_2,J_1}}\right)\sqrt{\frac{\beta_{I_2,J_1}}{\beta_{I_1,J_1}}}\frac{\Gamma(\alpha_{I_1,J_1}+\frac{1}{2})\Gamma(\alpha_{I_2,J_1}-\frac{1}{2})}{\Gamma(\alpha_{I_1,J_1})\Gamma(\alpha_{I_2,J_1})}\right].
\end{aligned} \tag{15}$$

Proof: See Appendix D. ■

Theorem 3 presents a closed-form expression of MSE_x, enabling efficient evaluation for the estimation accuracy. However, it is complex due to the involvement of Gamma functions and the complex coupling relationship between γ, K_x and K_y, making it difficult to gain insights. We then resort to a further asymptotic regime with large γ, where we have the following approximations: $\alpha_{I_i,J_1} \to \infty$, $\beta_{I_1,J_1} \approx \beta_{I_2,J_1}$ and $\lim_{z\to\infty}\frac{\Gamma(z+a)}{\Gamma(z)} \approx z^a$ [33, 5.11.12]. Hence, MSE_x can be further approximated into

$$\mathrm{MSE}_x \approx \frac{4\sin^4\phi_x}{\pi^2\sin^2\frac{\pi}{K_x}}\left[\frac{\alpha_{I_1,J_1}}{\alpha_{I_2,J_1}} - \frac{p^2_{I_1,J_1}}{p^2_{I_2,J_1}}\right], \tag{16}$$

taking the value of $\alpha_{i,j}$ into the above equation and performing some simple manipulations, we have

$$\mathrm{MSE}_x \approx \frac{4\sin^4\phi_x}{\pi^2\sin^2\frac{\pi}{K_x}}\left[\frac{2\sigma^2(p^2_{I_2,J_1}-p^2_{I_1,J_1})}{(p^2_{I_2,J_1}+2\sigma^2)p^2_{I_2,J_1}}\right]. \tag{17}$$

To this end, substituting $p_{i,j} = \sqrt{P_s}|\alpha_{\mathrm{cas}}u_iv_j|$ into the above equation, we see that MSE_x is inversely proportional to γ, indicating we can always improve the accuracy of angle estimation by increasing γ.

As the value of u_i in $p_{i,j}$ is related to $\theta_{1,x}$, we then propose to analyze the impact of K_x under a special case of $\theta_{1,x}$.

Corollary 1: In the high γ regime, when $\theta'_{1,x} = \frac{\pi}{K_x}$, MSE_x can be approximated as

$$\mathrm{MSE}_x \approx \frac{4K_x^2 \sin^2\frac{\pi}{2K_x}\tan^2\frac{\pi}{2K_x}\sigma^2}{2\pi^2|\alpha_{\text{cas}} v_{J_1}|^2 P_s}. \tag{18}$$

Proof: See Appendix E. ■

Observing Eq. (18), it is not an explicitly result to gain the impact of K_x. Therefore, we first extract the parts involving K_x and define $g(K_x) = K_x \sin\frac{\pi}{2K_x}\tan\frac{\pi}{2K_x}$. It is evident that $g(K_x) > 0$ as $K_x \geq 2$. Taking the derivate of $g(K_x)$ with respect to K_x and performing some simplifications, we have

$$g(K_x)' = \frac{\sin\frac{\pi}{2K_x}}{2K_x\cos^2\frac{\pi}{2K_x}}\left(K_x \sin\frac{\pi}{K_x} - \frac{\pi}{2}\cos\frac{\pi}{K_x} - \frac{3}{2}\pi\right). \tag{19}$$

Since the first item in the bracket can be regarded as a sinc function satisfying $\pi > K_x \sin\frac{\pi}{K_x}$, we can conclude that $g(K_x)' < 0$ and MSE_x decreases with K_x.

*Theorem 3*has discussed the close-form expression of MSE_x when $\theta_{1,x} \neq 0$, we will now continue the discussion for the case when $\theta_{1,x} = 0$.

Theorem 4: When $\theta_{1,x} = 0$, MSE_x can be accurately approximated as

$$\mathrm{MSE}_x \approx \frac{4\sin^2\frac{\pi}{K_x}}{\pi^2}\frac{\sigma^2\beta_{I_1,J_1}}{\alpha_{I_1,J_1} - 1}. \tag{20}$$

Proof: When $\theta_{1,x} = 0$, we have $\phi_x = 0$ and $z_{I_2,J_1} = 0$. In this case, we propose to use the first-order approximation $\lim_{\phi_x - \phi'_x \to 0}\frac{\tan\phi_x - \tan\phi'_x}{\phi_x - \phi'_x} \approx -\frac{1}{\cos^2\phi_x}$ to remove the arctan function involved in ϕ'_x. Hence, MSE_x can be approximated as

$$\mathrm{MSE}_x \approx \frac{4}{\pi^2}\mathbb{E}\left[\tan^2\phi'_x\right]. \tag{21}$$

Observing the fact that Z_{I_2,J_1} is negligible compared with Z_{I_1,J_1} when $\theta_{1,x} = 0$, $\tan\phi'_x$ can be approximated as $\tan\phi'_x \approx \frac{Z_{I_2,J_1}}{Z_{I_1,J_1}}\sin\frac{\pi}{K_x}$. To this stage, the mean of $\left(\frac{Z_{I_2,J_1}}{Z_{I_1,J_1}}\right)$ can be obtained in a similar way as the proof of Theorem 3, thus completing the proof. ■

Corollary 2: In the high γ regime, when $\theta_{1,x} = 0$, MSE_x can be approximated as

$$\mathrm{MSE}_x \approx \frac{4\sigma^2\sin^2\frac{\pi}{K_x}}{\pi^2|\alpha_{\text{cas}}|^2|v_{J_1}|^2 P_s}. \tag{22}$$

Corollary 2 can be easily proved and is omitted. It can be concluded that the MSE decreases with an increase in K_x and γ.

Remark: Based on *Theorem 3* and *Theorem 4*, we can conclude that MSE_x is inversely proportional to γ for arbitrary value of $\theta_{1,x}$ in the high SNR regime. This simple relationship between MSE_x and γ can be effectively used to guide the system design, such as beamforming and power allocation. It is important to note that most existing works utilize Cramer-Rao bound (CBR) as the performance indicator for system design [35], [36], [37], as the closed-form of MSE is difficult to obtain. However, using the CRB as an indicator may not result in optimal practical performance, and this paper provides a more accurate and simple performance indicator for the system design.

IV. The DoA-Assisted Detectors

The symbol detection in symbiotic radio systems typically requires the CSI [6], [7], [8], [9], [10], [11]. To avoid the unaffordable overhead for estimating secondary system's CSI, we propose to fully capture the characteristic of the ISAC systems and introduce two types of DoA-assisted detectors.

A. Reciprocal Linear Detectors

During the t-th symbol interval, the digital symbols of BS $D_{\mathrm{B},t} = 0$ and $D_{\mathrm{B},t} = 1$ are mapped into $s_{\mathrm{B},t} = -1$ and $s_{\mathrm{B},t} = 1$, respectively. The secondary (IRS) symbol bits $D_{\mathrm{I},t} \in \{0, 1\}$ are represented by $s_{\mathrm{I},t} = \pm 1$ with differential BPSK modulation, where symbol "1" represents the phase transition between adjacent symbols, while symbol "0" does not.

The receiving signal at time slot t can be expressed as

$$\begin{aligned}\mathbf{y}_{\mathrm{R},t} &= \sqrt{P_s}G_P\mathbf{h}_{\mathrm{BR}}s_{\mathrm{B},t} + \mathbf{n}_{\mathrm{R},t}\\ &\quad + \sqrt{P_s}\alpha_{\text{cas}}e^{-j2\pi v_{\mathrm{R}}t}s_{\mathrm{B},t}s_{\mathrm{I},t}\mathbf{a}_{K_x\times K_y}\left(\vartheta_{\mathrm{RI},x}, \vartheta_{\mathrm{RI},y}\right).\end{aligned} \tag{23}$$

Using the maximum-ratio-combining (MRC) or zero-forcing (ZF) combiner $\mathbf{f}$ with $\|\mathbf{f}\| = 1$, we have $y_{\mathrm{RC},t} = \mathbf{f}\mathbf{y}_{\mathrm{R},t}$, where

$$\mathbf{f} = \begin{cases}\dfrac{1}{K_xK_y}\mathbf{a}^H_{K_x\times K_y}\left(\dfrac{1}{K_xK_y}\vartheta_{\mathrm{RB},x}, \vartheta_{\mathrm{RB},y}\right), & \text{MRC},\\ \dfrac{1}{K_xK_y}\mathbf{a}^H_{K_x\times K_y}\left(\vartheta_{\mathrm{RI},x} + \dfrac{n_x}{K_x}, \vartheta_{\mathrm{RI},y} + \dfrac{n_x}{K_y}\right), & \text{ZF},\end{cases} \tag{24}$$

with $n_x = \arg\min_{n_x\in\{1,2,\ldots K_x-1\}}|\vartheta_{\mathrm{RI},x} + \frac{n_x}{K_x} - \vartheta_{\mathrm{RB},x}|$ and $n_y = \arg\min_{n_y\in\{1,2,\ldots K_y-1\}}|\vartheta_{\mathrm{RI},y} + \frac{n_y}{K_y} - \vartheta_{\mathrm{RB},y}|$ so as to maximize the energy of effective signal. We then decode the BS information as

$$\widehat{s_{\mathrm{B},t}} = \begin{cases}\dfrac{y_{\mathrm{RC},t}}{\alpha_{\mathrm{BR}}\sqrt{P_s}G_P}, & \text{MRC}.\\ \dfrac{K_xK_y y_{\mathrm{RC},t}}{\sqrt{P_s}G_P\mathbf{a}^H_{K_x\times K_y}\left(\vartheta_{\mathrm{RI},x} + \frac{n_x}{K_x}, \vartheta_{\mathrm{RI},y} + \frac{n_x}{K_y}\right)\mathbf{h}_{\mathrm{BR}}}, & \text{ZF}.\end{cases} \tag{25}$$

Subtracting the direct link signal from $\mathbf{y}_{\mathrm{R}}$ and assuming that optimal IRS phase shift $\boldsymbol{\theta}^*$ is used in the ensuing section, we can detect the equivalent IRS information as

$$\widehat{S_{\mathrm{I},t}} = \frac{\mathbf{a}^H_{K_x\times K_y}\left(\vartheta_{\mathrm{RI},x}, \vartheta_{\mathrm{RI},y}\right)\left(\mathbf{y}_{\mathrm{R},t} - \sqrt{P_s}G_P\mathbf{h}_{\mathrm{BR}}\widehat{s_{\mathrm{B},t}}\right)}{K_xK_y\sqrt{P_s}G_SN_xN_y\widehat{s_{\mathrm{B},t}}e^{-j2\pi v_{\mathrm{R}}t}}, \tag{26}$$

where $\widehat{S_{\mathrm{I},t}} = s_{\mathrm{I},t}\widehat{\alpha_{\mathrm{IR}}}\alpha_{\mathrm{IB}}$. Since the IRS moves along the belt, we treat the speed v_{R} a constant and known a prior. To further improve the detection performance of the primary systems, we incorporate $\mathrm{S}_{\mathrm{I},t}$ back into Eq. (23) and treat the reflect channel as multi-path gain. With this, $\mathrm{s}_{\mathrm{B},t}$ can be updated via

$$\widehat{\mathrm{s}_{\mathrm{B},t}}=\frac{\left[G_P\mathbf{h}_{\mathrm{BR}}+G_SN_xN_y\widehat{\mathrm{S}_{\mathrm{I},t}}\mathbf{a}_{K_x\times K_y}\left(\vartheta_{\mathrm{RI},x},\vartheta_{\mathrm{RI},y}\right)\right]^H\mathbf{y}_{\mathrm{R},t}}{\sqrt{P_s}\left\|G_P\mathbf{h}_{\mathrm{BR}}+G_SN_xN_y\widehat{\mathrm{S}_{\mathrm{I},t}}\mathbf{a}_{K_x\times K_y}(\vartheta_{\mathrm{RI},x},\vartheta_{\mathrm{RI},y})\right\|^2}. \tag{27}$$

Using the updated value of $\widehat{\mathrm{s}_{\mathrm{B},t}}$, $\widehat{\mathrm{S}_{\mathrm{I},t}}$ and $\widehat{\mathrm{s}_{\mathrm{B},t}}$ can be re-estimate via Eq. (26) and (27) iteratively until convergence. Based on the converged values $\widehat{\mathrm{S}_{\mathrm{I},t}}$ and $\widehat{\mathrm{s}_{\mathrm{B},t}}$, the binary symbols for BS and IRS can be obtained as

$$\widehat{\mathrm{D}_{\mathrm{B},t}}=\begin{cases}1, & \Re\left(\widehat{\mathrm{s}_{\mathrm{B},t}}\right)>0,\\ 0, & \Re\left(\widehat{\mathrm{s}_{\mathrm{B},t}}\right)<0,\end{cases} \tag{28}$$

and

$$\widehat{D_{\mathrm{I},t}}=\begin{cases}0, & \Re\left(\widehat{\mathrm{S}_{\mathrm{I},t-1}}\right)\Re\left(\widehat{\mathrm{S}_{\mathrm{I},t}}\right)\leq 0,\\ 1, & \Re\left(\widehat{\mathrm{S}_{\mathrm{I},t-1}}\right)\Re\left(\widehat{\mathrm{S}_{\mathrm{I},t}}\right)<0,\end{cases} \tag{29}$$

respectively.

B. Manchester Detector

The above reciprocal linear detectors can be regarded as heuristic ones that can either maximize the energy of effective signal or minimize the energy of the addictive interference, which are not optimal due to the addictive coupling between primary and secondary systems. To separate the primary and secondary signals, we propose to use the Manchester coding for IRS information, which is a binary coding strategy that encodes each bit of data as a transition between two voltage levels [38]. Specifically, the t-th IRS symbols $D_{\mathrm{I},t}\in\{0,1\}$ is coded by $s_{\mathrm{I},t}^{(1)}=\pm 1$ and $s_{\mathrm{I},t}^{(2)}=-s_{\mathrm{I},t}^{(1)}$, where $s_{\mathrm{I},t}^{(1)}$ and $s_{\mathrm{I},t}^{(2)}$ represent the IRS signal in the first and second half time of the symbol interval, and the corresponding receiving signal can be written as

$$\begin{aligned}&\mathbf{y}_{\mathrm{R},t}^{(1)}\\&=\sqrt{P_s}G_P\mathbf{h}_{\mathrm{BR}}\mathrm{s}_{\mathrm{B},t}+\mathbf{n}_{\mathrm{R},t}^{(1)}\\&\quad+\sqrt{P_s}G_S\alpha_{\mathrm{IR}}\alpha_{\mathrm{IB}}e^{j2\pi\mathrm{v}_{\mathrm{R}}t}N_xN_y\mathrm{s}_{\mathrm{B},t}\mathrm{s}_{\mathrm{I},t}^{(1)}\mathbf{a}_{K_x\times K_y}(\vartheta_{\mathrm{RI},x},\vartheta_{\mathrm{RI},y}),\end{aligned} \tag{30}$$

$$\begin{aligned}&\mathbf{y}_{\mathrm{R},t}^{(2)}\\&=\sqrt{P_s}G_P\mathbf{h}_{\mathrm{BR}}\mathrm{s}_{\mathrm{B},t}+\mathbf{n}_{\mathrm{R},t}^{(2)}\\&\quad-\sqrt{P_s}G_S\alpha_{\mathrm{IR}}\alpha_{\mathrm{IB}}e^{j2\pi\mathrm{v}_{\mathrm{R}}t}N_xN_y\mathrm{s}_{\mathrm{B},t}\mathrm{s}_{\mathrm{I},t}^{(1)}\mathbf{a}_{K_x\times K_y}(\vartheta_{\mathrm{RI},x},\vartheta_{\mathrm{RI},y}),\end{aligned} \tag{31}$$

respectively. Based on Eq. (30) and (31), we can separate the primary and secondary signals via

$$\begin{aligned}&\mathbf{y}_{\mathrm{R}}^{(1)}(t)+\mathbf{y}_{\mathrm{R}}^{(2)}(t)\\&=2\sqrt{P_s}G_P\mathbf{h}_{\mathrm{BR}}\mathrm{s}_{\mathrm{B},t}+\mathbf{n}_{\mathrm{R,t}}^{(1)}+\mathbf{n}_{\mathrm{R},t}^{(2)},\end{aligned} \tag{32}$$

$$\begin{aligned}&\mathbf{y}_{\mathrm{R}}^{(1)}(t)-\mathbf{y}_{\mathrm{R}}^{(2)}(t)\\&=\mathbf{n}_{\mathrm{R,t}}^{(1)}-\mathbf{n}_{\mathrm{R,t}}^{(2)}\\&\quad+2\sqrt{P_s}G_S|\alpha_{\mathrm{IR}}\alpha_{\mathrm{IB}}|N_xN_y\mathrm{s}_{\mathrm{B},t}\mathrm{s}_{\mathrm{I},t}^{(1)}\mathbf{a}_{K_x\times K_y}\left(\vartheta_{\mathrm{RI},x},\vartheta_{\mathrm{RI},y}\right),\end{aligned} \tag{33}$$

where the first equation involves only primary signal, whereas the second equation contains the secondary signal. To this stage, the BS signal can be obtained as follows

$$\widehat{\mathrm{s}_{\mathrm{B},t}}=\frac{1}{2\sqrt{P_s}G_P}\frac{\mathbf{h}_{\mathrm{BR}}^H}{|\mathbf{h}_{\mathrm{BR}}|^2}\left(\mathbf{y}_{\mathrm{R},t}^{(1)}+\mathbf{y}_{\mathrm{R},t}^{(2)}\right), \tag{34}$$

and can be mapped into digital domain as

$$\widehat{\mathrm{D}_{\mathrm{B},t}}=\begin{cases}1, & \Re\left(\widehat{\mathrm{s}_{\mathrm{B},t}}\right)>0.\\ -1, & \Re\left(\widehat{\mathrm{s}_{\mathrm{B},t}}\right)<0.\end{cases} \tag{35}$$

Using the obtained $\mathrm{s}_{\mathrm{B},t}$, the equivalent IRS signal can be obtained as

$$\widehat{\alpha_{\mathrm{IR}}\alpha_{\mathrm{IB}}\mathrm{s}_{\mathrm{I},t}^{(1)}}=\frac{\mathbf{a}_{K_x\times K_y}^H\left(\widehat{\vartheta_{\mathrm{RI},x}},\widehat{\vartheta_{\mathrm{RI},y}}\right)}{2\sqrt{P_s}G_SK_xK_yN_xN_y\widehat{\mathrm{s}_{\mathrm{B},t}}}\left(\mathbf{y}_{\mathrm{R},t}^{(1)}-\mathbf{y}_{\mathrm{R},t}^{(2)}\right). \tag{36}$$

To avoid the trouble of unknown channel path gain, we assume that the IRS symbols are with differential Manchester coding. In this case, the binary bits can be obtained by calculating the correlation coefficient between the current time $\widehat{\alpha_{\mathrm{IR}}\alpha_{\mathrm{IB}}\mathrm{s}_{\mathrm{I},t}^{(1)}}$ and the previous time $\widehat{\alpha_{\mathrm{IR}}\alpha_{\mathrm{IB}}\mathrm{s}_{\mathrm{I},t-1}^{(1)}}$. Specifically, the t-th IRS symbol D_{t} can be obtained as

$$\widehat{D_{\mathrm{I},t}}=\begin{cases}0, & \Re\left(\widehat{\alpha_{\mathrm{IR}}\alpha_{\mathrm{IB}}\mathrm{s}_{\mathrm{I},t-1}^{(1)}}\right)\Re\left(\widehat{\alpha_{\mathrm{IR}}^H\alpha_{\mathrm{IB}}^H\mathrm{s}_{\mathrm{I},t}^{(1)}}\right)\leq 0.\\ 1, & \Re\left(\widehat{\alpha_{\mathrm{IR}}\alpha_{\mathrm{IB}}\mathrm{s}_{\mathrm{I},t-1}^{(1)}}\right)\Re\left(\widehat{\alpha_{\mathrm{IR}}^H\alpha_{\mathrm{IB}}^H\mathrm{s}_{\mathrm{I},t}^{(1)}}\right)<0.\end{cases} \tag{37}$$

Remark: Compared to the case with perfect CSI, there is about a 3dB performance loss for the IRS symbols due to the error propagation caused by differential coding.

V. Numerical Results

In this section, the numerical results are provided to evaluate the efficacy of the proposed DoA estimator and DoA-assisted detectors, as well as validate the theoretical analysis. Unless explicitly stated, we set the number of receiver antenna as $K_x=K_y=8$, the number of IRS reflecting elements as $N_x=N_y=8$, the path gain of the channels as $|\alpha_{\mathrm{IR}}|=|\alpha_{\mathrm{IB}}|=0.1$.

A. The Performance of the Ratio-DPML Based DoA Estimator

Fig.3 depicts the effective sensing probability $\mathrm{P}_{\mathrm{eff}}$ and examines the accuracy of the approximation $\mathrm{P}_{\mathrm{eff}}^{\infty}$ when $\theta_{1,x}=\theta_{1,y}=\frac{0.6}{K}$ and $K=K_x=K_y$. As illustrated, we see that the accuracy of $\mathrm{P}_{\mathrm{eff}}^{\infty}$ gradually improves with the increasing of SNR, thereby validating the effectiveness of the analytical results. Comparing the curves with different K, it can be seen that $\mathrm{P}_{\mathrm{eff}}$ monotonically increases with K and SNR, and eventually converges 1 as K and/or SNR becomes large, indicating that we can always guarantee that the correct value of I_1, I_2, J_1 and J_2 can be reliably identified in the high SNR or large K regime.

Fig. 4 investigates the impact of the number of IRS elements and receiving antennas on the MSE performance.

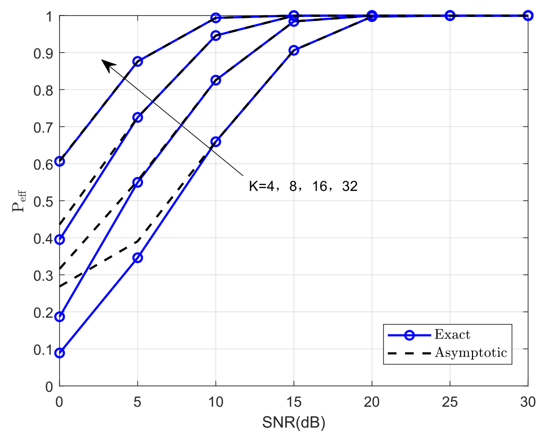

Fig. 3. Effective sensing probability.

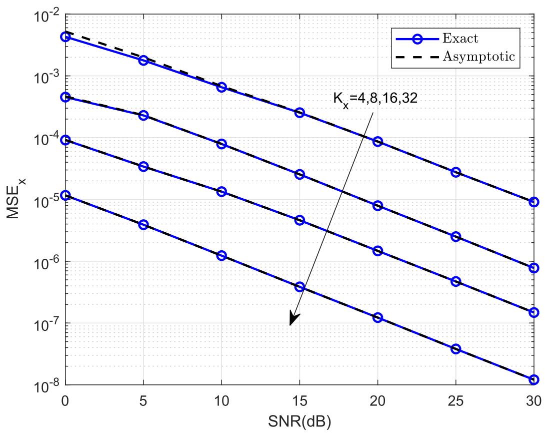

(a) Impact of K_x on $\mathrm{MSE_x}$.

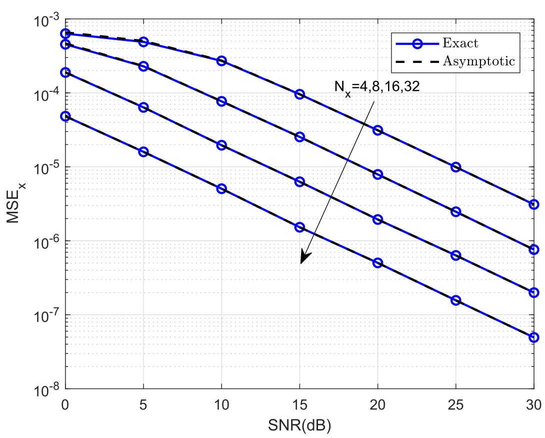

(b) Impact of N_x on $\mathrm{MSE_x}$.

Fig. 4. Impact of K_x and N_x on $\mathrm{MSE_x}$.

Without loss of generality, we presents the results of MSE_x for the purpose of illustration. As can be readily observed, the asymptotic results are tightly aligned with the numerical results in the high SNR regime and MSE_x decreases linearly with SNR, which is consistent with the theoretical analysis. Moreover, we see that MSE_x decreases with the increasing of K_x and N_x.

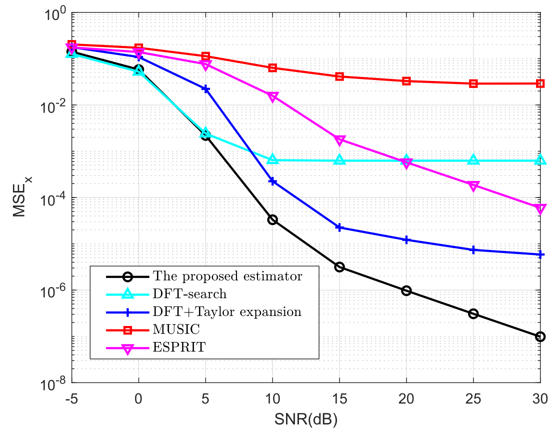

Fig. 5. Comparison between the DoA estimators.

Fig. 5 compares the MSE performance of the proposed Ratio-DPML based DoA estimator with several benchmarks, including the traditional DFT-search method, DFT method with Taylor expansion, MUSIC method and ESPRIT method. Without lose of generality, we set $K_x = 16$, $\vartheta_{\mathrm{RI},x} = \frac{2.6}{K_x}$ and equal number of searches for all means. We see that the proposed sensing method outperforms the DFT method with Taylor expansion, MUSIC and ESPRIT methods for the entire range of SNR, while inferior to the DFT-search method in the low SNR regime. This phenomenon can be explained as follows: Since the proposed Ratio-DPML based DoA estimator requires both the peak and the second-largest value of the DFT spectrum, where the second-largest value is susceptible to the noise in the low SNR regime, thereby resulting in higher error compared to the DFT-search method that uses only the largest value. However, the accuracy of the DFT-search method is severely limited by the number of searches, whereas the MSE of the proposed Ratio-DPML based DoA estimator decreases with SNR without floor. Overall, the above results highlight the superior performance of the proposed DoA estimator compared to several benchmark methods.

B. The Performance of the Proposed DoA-Assisted Detectors

Fig.6 illustrates the convergence behavior of the reciprocal linear detectors when $\gamma = 5$dB and $K_x = K_y = N_x = N_y = 4$. As the estimated values of $\widehat{\mathrm{s}_{\mathrm{B},t}}$ and $\widehat{\mathrm{S}_{\mathrm{I},t}}$ are usually complex numbers, we propose to evaluate the convergence by using the normalized amplitude as the objective value, i.e., $|\widehat{\mathrm{s}_{\mathrm{B},t}}|$ and $|\widehat{\mathrm{S}_{\mathrm{I},t}}|/|\alpha_{\mathrm{IR}}\alpha_{\mathrm{IB}}|$. It is evident that the objective values using both MRC and ZF combiners converge to the same values after several iterations, indicating that the reciprocal linear detectors can achieve similar detection performance after convergence.

Fig. 7 compares the BER performance between the proposed reciprocal linear detector (RLD) and Manchester detector (MD) for both primary (Pri) and secondary (Sec) systems with imperfect/perfect DoA information or perfect CSI when $K_x = K_y = N_x = N_y = 4$. The error of the DoA is set in order of 10^{-2}. Obviously, we see that the BER of both primary and secondary transmission for Manchester detector is lower than that of the reciprocal linear detectors, since the former can separate the primary and secondary signal completely. In addition, we see that the BER for the primary transmission

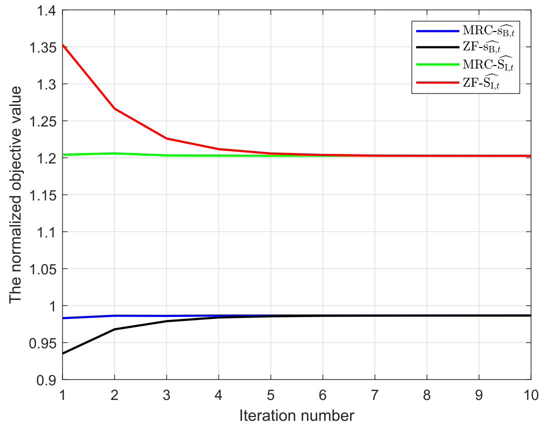

Fig. 6. Convergence of the reciprocal linear detector.

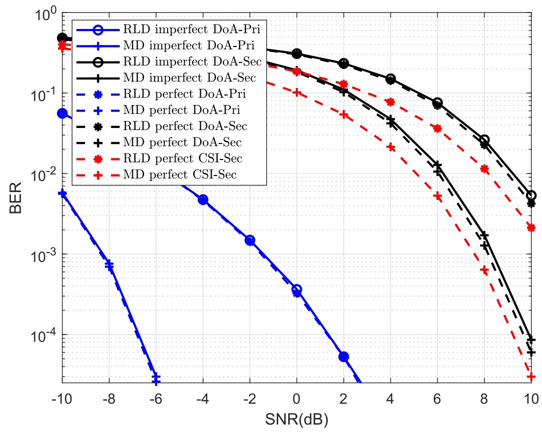

Fig. 7. Performance of the proposed DoA-assisted detectors.

is much lower than that of the secondary transmission due to the larger equivalent channel path gain. Comparing the performance of the detectors with imperfect and perfect DoA, we see that there exists slightly performance loss with DoA errors. Moreover, the BER performance of secondary transmission with perfect DoA has about 3dB performance loss compared with that of the perfect CSI scenario, for the fact that the differential coding would results the error propagation between adjacent symbols.

VI. Conclusion

This paper investigated the integrated location sensing via DoA estimation and DoA-assisted symbol detection for symbiotic radio systems. Specifically, a timely and low-complexity 2D DoA estimator based on Ratio-DPML by using a single snapshot and a UPA receiver was proposed. By analyzing the effective sensing probability and MSE of the proposed estimator, we found that the estimation accuracy improves with the increasing γ, K_x and K_y. Moreover, the numerical results showed that the proposed estimator can achieve high accuracy with limited searches and outperforms several benchmarks. To eliminate the dependency of symbol detection on CSI, two types of DoA-assisted detectors, specifically, the reciprocal linear detectors and a Manchester detector, were proposed. The numerical results were presented to validate the efficacy of the proposed DoA-assisted detectors. It can be seen that the reciprocal linear detectors with MRC and ZF combiners can achieve similar detection performance after convergence, and the Manchester detector outperforms the reciprocal linear detectors due to the interference cancellation, while has about 3dB BER loss compared with perfect CSI scenario. The above results demonstrated that the ISAC can be achieved for symbiotic radio systems by properly leveraging the resource and information sharing mechanisms, making high-energy and -spectrum efficiency IoT networks a possible.

Appendix A
Proof of Lemma 1

According to the formula of summation for geometric sequence, $z_{i,j}$ of arbitrary column j can be calculated as

$$z_{i,j} = \frac{\sqrt{P_s}|\alpha_{\text{cas}} s_{\text{B}} s_{\text{I}} v_j|}{K_x}\left|\frac{\sin\frac{\pi}{2}K_x\theta}{\sin\frac{\pi}{2}\theta}\right|, \tag{38}$$

where $\theta = \vartheta_{\text{BR},x} + \frac{2(i-1)}{K_x} - \vartheta_{\text{RI},x}$. It is evident that $0 = \arg\max_\theta z_{i,j}$, but it cannot be guaranteed that there exists an $i \in \mathbb{N}$ such that $\vartheta_{\text{BR},x} + \frac{2(i-1)}{K_x} - \vartheta_{\text{RI},x} = 0$. Denote $i_1 = \arg\max_{i=1,\ldots K_x} z_{i,j}$ and the corresponding $\theta_{1,x} = \vartheta_{\text{BR},x} + \frac{2(i_1-1)}{K_x} - \vartheta_{\text{RI},x}$, we can guarantee that i_1 can always make $\theta_{1,x} \in [-\frac{1}{K_x}, \frac{1}{K_x}]$. Without loss of generality, assuming $\theta_{1,x} \in [-\frac{1}{K_x}, 0]$, the other equivalent angle on the main lobe of the column j can be expressed as $\theta_{2,x} = \theta_{1,x} + \frac{2}{K_x}$,[7] with function value

$$z_{i_2,j} = \frac{\sqrt{P_s}|\alpha_{\text{cas}} s_{\text{B}} s_{\text{I}} v_j|}{K_x}\left|\frac{\sin\frac{\pi}{2}K_x\theta_{1,x}}{\sin\frac{\pi}{2}(\theta_{1,x}+\frac{2}{K_x})}\right|. \tag{39}$$

Obviously, $z_{i_1,j} \geq z_{i_2,j}$ since $\theta_{1,x} \in [-\frac{1}{K_x}, 0]$. The equivalent angle on the side lobe that nearest to $\theta_{1,x}$ can be obtain by $\theta_{3,x} = \theta_{1,x} - \frac{2}{K_x}$, with function value

$$z_{i_3,j} = \frac{\sqrt{P_s}|\alpha_{\text{cas}} s_{\text{B}} s_{\text{I}} v_j|}{K_x}\left|\frac{\sin\frac{\pi}{2}K_x\theta_{1,x}}{\sin\frac{\pi}{2}(\theta_{1,x}-\frac{2}{K_x})}\right|. \tag{40}$$

Since $\theta_{1,x} \in [-\frac{1}{K_x}, 0]$ and $K_x \geq 3$, we have $z_{i_2,j} > z_{i_3,j}$, which yields the desired result. The analysis for arbitrary row i is similar and omitted.

Appendix B
Proof of Theorem 1

Since the two points on the main lobe satisfying $-\frac{1}{K_x} \leq \theta_{1,x} < 0 < \theta_{2,x}$ and $\theta_{1,x} + \frac{2}{K_x} = \theta_{2,x}$, we have the ratio of z_{i_1,j_1} and z_{i_2,j_1} as

$$\frac{z_{i_2,j_1}}{z_{i_1,j_1}} = \left|\frac{\sin\frac{\pi}{2}\theta_{1,x}}{\sin\frac{\pi}{2}(\theta_{1,x}+\frac{2}{K_x})}\right|, \tag{41}$$

Since $\theta_{1,x} \in [-\frac{1}{K_x}, 0]$ and $K_x \geq 3$, we have $\sin\frac{\pi}{2}(\theta_{1,x} + \frac{2}{K_x}) > 0$ and $\sin\frac{\pi}{2}\theta_{1,x} < 0$, thus with some simple manipulations, Eq. (41) can be simplified as

$$\left(z_{i_1,j_1} + z_{i_2,j_1}\cos\frac{\pi}{K_x}\right)\sin\frac{\pi}{2}\theta_{1,x} + \Delta_x z_{i_2,j_1}\sin\frac{\pi}{K_x}\cos\frac{\pi}{2}\theta_{1,x} = 0. \tag{42}$$

[7]Note that since the DFT spectrum is periodic with 1, when $i_1 = 1$, we have $z_{i_2,j} = z_{K_x-1,j}$; when $i_1 = K_x$, let $z_{i_3,j} = Z_{1,j}$.

Let $\tan\phi_x = \frac{\Delta_x z_{i_2,j_1} \sin\frac{\pi}{K_x}}{z_{i_1,j_1}+z_{i_2,j_1}\cos\frac{\pi}{K_x}}$, the above equation can be rewritten as

$$\cos\phi_x \sin\frac{\pi}{2}\theta_{1,x} + \sin\phi_x \cos\frac{\pi}{2}\theta_{1,x} = 0, \tag{43}$$

hence we have $\frac{\pi}{2}\theta_{1,x} + \phi_x = k_x\pi$. To this end, combining $\theta_{1,x} = \vartheta_{\mathrm{BR},x} + \frac{2(i_1-1)}{K_x} - \vartheta_{\mathrm{RI},x}$ yields the desired result.

Appendix C
The Proof of Theorem 2

With noise, $Z_{i,j}$ can be written as

$$Z_{i,j} = \left|\sqrt{P_s}\alpha_{\mathrm{cas}} s_{\mathrm{B}} s_{\mathrm{I}} u_i v_j + n_{i,j}\right|, \tag{44}$$

which is independent of arbitrary $Z_{i',j'}$ when $i \neq i'$ and $j \neq j'$. Obviously, $Z_{i,j}$ follows Rician distribution, however its probability density function (PDF) is complicated and makes the ensuing analysis intrackable. It is worth noting that $Z_{i,j}^2$ is the sum of two non-central chi-square variables, which can be approximated as a gamma distribution [39]. Since the square root of gamma distribution follows Nakagami distribution [40], we have $Z_{i,j} \sim \mathrm{Na}(\alpha_{i,j}, \beta_{i,j})$ with PDF

$$f_{Z_{i,j}}(x) = \frac{2\beta_{i,j}^{\alpha_{i,j}}}{\Gamma(\alpha_{i,j})} x^{2\alpha_{i,j}-1} \mathrm{e}^{-\beta_{i,j}x^2}. \tag{45}$$

Define $\mathrm{Rat}_{\mathrm{I}_2,\mathrm{I}_3} = \frac{Z_{I_2,J_1}}{Z_{I_3,J_1}}$, the PDF of $\mathrm{Rat}_{\mathrm{I}_2,\mathrm{I}_3}$ can be derived as

$$f_{\mathrm{Rat}_{\mathrm{I}_2,\mathrm{I}_3}}(r) = \int_0^\infty t f_{Z_{I_2,J_1}}(rt) f_{Z_{I_3,J_1}}(t)\mathrm{d}t \tag{46}$$

taking the distribution of $f_{Z_{I_2,J_1}}(t)$ and $f_{Z_{I_3,J_1}}(t)$ into the above equation and using the relationship in [34, Eq. 3.326.2], we have

$$f_{\mathrm{Rat}_{\mathrm{I}_2,\mathrm{I}_3}}(r) = \frac{2\beta_{I_3,J_1}^{\alpha_{I_3,J_1}} \beta_{I_2,J_1}^{\alpha_{I_2,J_1}} \Gamma(\alpha_{I_3,J_1}+\alpha_{I_2,J_1})}{\Gamma(\alpha_{I_3,J_1})\Gamma(\alpha_{I_2,J_1})} \times \frac{z^{2\alpha_{I_2,J_1}-1}}{(\beta_{I_2,J_1}z^2+\beta_{I_3,J_1})^{\alpha_{I_3,J_1}+\alpha_{I_2,J_1}}}. \tag{47}$$

To this end, $\Pr\left[\frac{Z_{I_2,J_1}}{Z_{I_3,J_1}} \geq 1\right]$ can be regarded as the cumulative distribution function (CDF) of $f_{\mathrm{Rat}_{\mathrm{I}_2,\mathrm{I}_3}}(r)$. Making a change of variable $z = \sqrt{t}$, $\Pr\left[\frac{Z_{I_2,J_1}}{Z_{I_3,J_1}} \geq 1\right]$ can be computed as

$$\Pr\left[\frac{Z_{I_2,J_1}}{Z_{I_3,J_1}} \geq 1\right] = \frac{\Gamma(\alpha_{I_3,J_1}+\alpha_{I_2,J_1})}{\Gamma(\alpha_{I_3,J_1})\Gamma(\alpha_{I_2,J_1})} \left(\frac{\beta_{I_2,J_1}}{\beta_{I_3,J_1}}\right)^{\alpha_{I_2,J_1}} \times \int_1^\infty \frac{t^{\alpha_{I_2,J_1}-1}}{(\frac{\beta_{I_2,J_1}}{\beta_{I_3,J_1}}t+1)^{\alpha_{I_3,J_1}+\alpha_{I_2,J_1}}}\mathrm{d}t. \tag{48}$$

Invoking the integration formula [34, Eq. 3.194.2], the above equation can be calculated as

$$\begin{aligned}&\Pr\left[\frac{Z_{I_2,J_1}}{Z_{I_3,J_1}} \geq 1\right]\\ &= \frac{\Gamma(\alpha_{I_3,J_1}+\alpha_{I_2,J_1})}{\Gamma(\alpha_{I_3,J_1}+1)\Gamma(\alpha_{I_2,J_1})} \left(\frac{\beta_{I_3,J_1}}{\beta_{I_2,J_1}}\right)^{\alpha_{I_3,J_1}}\\ &\times {}_2F_1\left(\alpha_{I_2,J_1}+\alpha_{I_3,J_1}, \alpha_{I_3,J_1}; \alpha_{I_3,J_1}+1; -\frac{\beta_{I_3,J_1}}{\beta_{I_2,J_1}}\right).\end{aligned}$$

The result for $\Pr\left[\frac{Z_{I_1,J_2}}{Z_{I_1,J_3}} \geq 1\right]$ can be similarly obtained. To this end, pulling $\Pr\left[\frac{Z_{I_2,J_1}}{Z_{I_3,J_1}} \geq 1\right]$ and $\Pr\left[\frac{Z_{I_1,J_2}}{Z_{I_1,J_3}} \geq 1\right]$ together yields yields the desired result.

Appendix D
The Proof of Theorem 3

Invoking Eq. (12) and (13), the MSE for $\vartheta_{\mathrm{RI},x}$ can be expressed as

$$\mathrm{MSE}_x \triangleq \mathbb{E}\left[|\vartheta_{\mathrm{RI},x} - \widehat{\vartheta_{\mathrm{RI},x}}|^2\right] = \frac{4}{\pi^2}\mathbb{E}\left[|\phi_x - \phi_x'|^2\right]. \tag{49}$$

Obviously, the error mainly comes from obtaining ϕ_x' based on Z_{I_1,J_1} and Z_{I_2,J_1}. Note that when $\theta_{1,x} \neq 0$, we have $z_{I_2,J_1} \neq 0$ and ϕ_x' can also be written as $\phi_x' = \operatorname{arccot}\left(\Delta_x \frac{Z_{I_1,J_1}}{Z_{I_2,J_1}\sin\frac{\pi}{K_x}} + \Delta_x \cot\frac{\pi}{K_x}\right)$. It is hard to analyze the statistical characteristics of ϕ_x' directly due to the involvement of arccot function, hence we propose to use the first-order approximation $\frac{\cot\phi_x - \cot\phi_x'}{\phi_x - \phi_x'} \approx -\frac{1}{\sin^2\phi_x}$, $\phi_x \neq 0$, to remove the arccot function.[8] As such, MSE_x can be approximated as

$$\mathrm{MSE}_x \approx \frac{4\sin^4\phi_x}{\pi^2}\mathbb{E}\left[(\cot\phi_x - \cot\phi_x')^2\right]. \tag{50}$$

Taking the value of $\cot\phi_x = \Delta_x \frac{z_{I_1,J_1}}{z_{I_2,J_1}\sin\frac{\pi}{K_x}} + \Delta_x \cot\frac{\pi}{K_x}$ and $\cot\phi_x' = \Delta_x \frac{Z_{I_1,J_1}}{Z_{I_2,J_1}\sin\frac{\pi}{K_x}} + \Delta_x \cot\frac{\pi}{K_x}$ into Eq. (50), MSE_x can be further written as

$$\mathrm{MSE}_x \approx \frac{4\sin^4\phi_x}{\pi^2\sin^2\frac{\pi}{K_x}}\mathbb{E}\left[\left(\frac{Z_{I_1,J_1}}{Z_{I_2,J_1}} - \frac{z_{I_1,J_1}}{z_{I_2,J_1}}\right)^2\right], \tag{51}$$

where the expectation part can be expanded as

$$\begin{aligned}\mathbb{E}\left[\left(\frac{Z_{I_1,J_1}}{Z_{I_2,J_1}} - \frac{z_{I_1,J_1}}{z_{I_2,J_1}}\right)^2\right] &= \mathbb{E}\left[\left(\frac{Z_{I_1,J_1}}{Z_{I_2,J_1}}\right)^2\right] + \left(\frac{p_{I_1,J_1}}{p_{I_2,J_1}}\right)^2\\ &\quad - 2\frac{p_{I_1,J_1}}{p_{I_2,J_1}} E\left[\left(\frac{Z_{I_1,J_1}}{Z_{I_2,J_1}}\right)\right].\end{aligned} \tag{52}$$

The remaining task is to obtain $\mathbb{E}\left[\left(\frac{Z_{I_1,J_1}}{Z_{I_2,J_1}}\right)^2\right]$ and $\mathbb{E}\left[\frac{Z_{I_1,J_1}}{Z_{I_2,J_1}}\right]$.

1) Obtaining $\mathbb{E}\left[\frac{Z_{I_1,J_1}}{Z_{I_2,J_1}}\right]$: First of all, the PDF of $f_{\mathrm{Rat}_{\mathrm{I}_1,\mathrm{I}_2}}(z)$ can be similar derived as $f_{\mathrm{Rat}_{\mathrm{I}_2,\mathrm{I}_3}}(z)$, thus, the mean of $\frac{Z_{I_1,J_1}}{Z_{I_2,J_1}}$ can be calculated via

$$\mathbb{E}\left[\frac{Z_{I_1,J_1}}{Z_{I_2,J_1}}\right] = \int_0^\infty f_{\mathrm{Rat}_{\mathrm{I}_1,\mathrm{I}_2}}(z) z \mathrm{d}z. \tag{53}$$

Taking the expression of $f_{\mathrm{Rat}_{\mathrm{I}_1,\mathrm{I}_2}}(z)$ into Eq. (53) and letting $z = \sqrt{t}$, the above equation can be obtained as

$$\mathbb{E}\left[\frac{Z_{I_1,J_1}}{Z_{I_2,J_1}}\right] = \frac{\Gamma(\alpha_{I_2,J_1}+\alpha_{I_1,J_1})}{\Gamma(\alpha_{I_2,J_1})\Gamma(\alpha_{I_1,J_1})}\left(\frac{\beta_{I_1,J_1}}{\beta_{I_2,J_1}}\right)^{\alpha_{I_1,J_1}} \times \int_0^\infty \frac{t^{\alpha_{I_1,J_1}-\frac{1}{2}}}{(\frac{\beta_{I_1,J_1}}{\beta_{I_2,J_1}}t+1)^{\alpha_{I_2,J_1}+\alpha_{I_1,J_1}}}\mathrm{d}t, \tag{54}$$

[8] The accuracy of the approximation increases with the decreasing $\phi_x' - \phi_x$.

using the integration relationship in [34, Eq. 3.194.1] and performing some simple manipulations, we have

$$\mathbb{E}\left[\frac{Z_{I_1,J_1}}{Z_{I_2,J_1}}\right]=\frac{\Gamma(\alpha_{I_1,J_1}+\frac{1}{2})\Gamma(\alpha_{I_2,J_1}-\frac{1}{2})}{\Gamma(\alpha_{I_1,J_1})\Gamma(\alpha_{I_2,J_1})}\left(\frac{\beta_{I_2,J_1}}{\beta_{I_1,J_1}}\right)^{\frac{1}{2}}. \quad (55)$$

2) Obtaining $\mathbb{E}\left[\left(\frac{Z_{I_1,J_1}}{Z_{I_2,J_1}}\right)^2\right]$: $Z^2_{I_1,J_1}$ can be approximated by Gamma distribution with mean $\mathbb{E}[Z^2_{I_1,J_1}] = p^2_{I_1,J_1} + \sigma^2$ and variance $\mathbb{D}[Z^2_{I_1,J_1}] = 2p^2_{I_1,J_1}\sigma^2 + \sigma^4$. According to the conclusion in [41], the ratio of $Z^2_{I_1,J_1}$ and $Z^2_{I_2,J_1}$ follows the Beta prime distribution, namely, $\left(\frac{Z_{I_1,J_1}}{Z_{I_2,J_1}}\right)^2 \sim \beta'(\alpha_{I_1,J_1}, \alpha_{I_2,J_1}, 1, \frac{\beta_{I_2,J_1}}{\beta_{I_1,J_1}})$, whose mean can be derived based on ready-made conclusion as

$$\mathbb{E}\left[\left(\frac{Z_{I_1,J_1}}{Z_{I_2,J_1}}\right)^2\right] = \frac{\alpha_{I_1,J_1}\beta_{I_2,J_1}}{(\alpha_{I_2,J_1}-1)\beta_{I_1,J_1}}. \quad (56)$$

To this end, pulling Eq. (51), (52), (55) and (56) all together yields the desired result.

Appendix E
The Proof of Corollary 1

When $\theta_{1,x} = \frac{\pi}{K_x}$, we have $z_{I_1,J_1} = z_{I_2,J_1}$, $\alpha_{I_1,J_1} = \alpha_{I_2,J_1}$ and $\beta_{I_1,J_1} = \beta_{I_2,J_1}$. The Eq. (52) can be further simplified as

$$\mathbb{E}\left[\left(\frac{Z_{I_1,J_1}}{Z_{I_2,J_1}} - \frac{z_{I_1,J_1}}{z_{I_2,J_1}}\right)^2\right] \approx \frac{1}{\alpha_{I_1,J_1}-1}. \quad (57)$$

Recalling α_{I_1,J_1}, it can be expanded as

$$\alpha_{I_1,J_1} = \frac{\left(|\alpha_{\text{cas}}u_{I_1}v_{J_1}|^2P_s+\sigma^2\right)^2}{2|\alpha_{\text{cas}}u_{I_1}v_{J_1}|^2P_s\sigma^2+\sigma^4}, \quad (58)$$

further, taking $|u_{I_1}| = \frac{1}{K_x \sin\frac{\pi}{2K_x}}$ into α_{I_1,J_1}, we have

$$\alpha_{I_1,J_1}=\frac{|\alpha_{\text{cas}}|^4{P_s}^2|v_{J_1}|^4}{2|\alpha_{\text{cas}}|^2K_x^2\sin^2\frac{\pi}{2K_x}P_s|v_{J_1}|^2\sigma^2+\sigma^4K_x^4\sin^4\frac{\pi}{2K_x}}+1. \quad (59)$$

When SNR is large, Eq. (59) can be approximated and simplified as

$$\alpha_{I_1,J_1} \approx \frac{|\alpha_{\text{cas}}|^2P_s|v_{J_1}|^2}{2K_x^2\sin^2\frac{\pi}{2K_x}\sigma^2}+1. \quad (60)$$

To this end, taking Eq. (57) and (60) into (51) yields the desired result.

References

[1] R. Long, Y.-C. Liang, H. Guo, G. Yang, and R. Zhang, "Symbiotic radio: A new communication paradigm for passive Internet of Things," *IEEE Internet Things J.*, vol. 7, no. 2, pp. 1350–1363, Feb. 2020.

[2] Q. Zhang, Y.-C. Liang, H.-C. Yang, and H. V. Poor, "Mutualistic mechanism in symbiotic radios: When can the primary and secondary transmissions be mutually beneficial?" *IEEE Trans. Wireless Commun.*, vol. 21, no. 10, pp. 8036–8050, Oct. 2022.

[3] Y.-C. Liang, Q. Zhang, E. G. Larsson, and G. Y. Li, "Symbiotic radio: Cognitive backscattering communications for future wireless networks," *IEEE Trans. Cognit. Commun. Netw.*, vol. 6, no. 4, pp. 1242–1255, Dec. 2020.

[4] G. Yang, Q. Zhang, and Y.-C. Liang, "Cooperative ambient backscatter communications for green Internet-of-Things," *IEEE Internet Things J.*, vol. 5, no. 2, pp. 1116–1130, Apr. 2018.

[5] S. Zhang and R. Zhang, "Intelligent reflecting surface aided multi-user communication: Capacity region and deployment strategy," *IEEE Trans. Commun.*, vol. 69, no. 9, pp. 5790–5806, Sep. 2021.

[6] Q. Tao, S. Zhang, C. Zhong, and Y. Zhang, "Joint information transmission design for intelligent reflecting surface aided system with discrete phase shifts," *Sci. China Inf. Sci.*, vol. 66, no. 3, pp. 1–10, Feb. 2023.

[7] M. Wu, X. Lei, X. Zhou, Y. Xiao, X. Tang, and R. Hu, "Reconfigurable intelligent surface assisted spatial modulation for symbiotic radio," *IEEE Trans. Veh. Technol.*, vol. 70, no. 12, pp. 12918–12931, Dec. 2021.

[8] E. Basar, "Reconfigurable intelligent surface-based index modulation: A new beyond MIMO paradigm for 6G," *IEEE Trans. Commun.*, vol. 68, no. 5, pp. 3187–3196, May 2020.

[9] W. Yan, X. Yuan, and X. Kuai, "Passive beamforming and information transfer via large intelligent surface," *IEEE Wireless Commun. Lett.*, vol. 9, no. 4, pp. 533–537, Apr. 2020.

[10] W. Yan, X. Yuan, Z.-Q. He, and X. Kuai, "Passive beamforming and information transfer design for reconfigurable intelligent surfaces aided multiuser MIMO systems," *IEEE J. Sel. Areas Commun.*, vol. 38, no. 8, pp. 1793–1808, Aug. 2020.

[11] Y. Ma, R. Liu, M. Li, and Q. Liu, "Passive information transmission in intelligent reflecting surface aided MISO systems," *IEEE Commun. Lett.*, vol. 24, no. 12, pp. 2951–2955, Dec. 2020.

[12] C. You, B. Zheng, and R. Zhang, "Channel estimation and passive beamforming for intelligent reflecting surface: Discrete phase shift and progressive refinement," *IEEE J. Sel. Areas Commun.*, vol. 38, no. 11, pp. 2604–2620, Nov. 2020.

[13] Q. Zhang, H. Guo, Y.-C. Liang, and X. Yuan, "Constellation learning-based signal detection for ambient backscatter communication systems," *IEEE J. Sel. Areas Commun.*, vol. 37, no. 2, pp. 452–463, Feb. 2019.

[14] J. A. Zhang et al., "Enabling joint communication and radar sensing in mobile networks—A survey," *IEEE Commun. Surveys Tuts.*, vol. 24, no. 1, pp. 306–345, 1st Quart., 2022.

[15] R. Schmidt, "Multiple emitter location and signal parameter estimation," *IEEE Trans. Antennas Propag.*, vol. AP-34, no. 3, pp. 276–280, Mar. 1986.

[16] F. Gao and A. B. Gershman, "A generalized ESPRIT approach to direction-of-arrival estimation," *IEEE Signal Process. Lett.*, vol. 12, no. 3, pp. 254–257, Mar. 2005.

[17] W. Zhao, G. Wang, S. Atapattu, R. He, and Y.-C. Liang, "Channel estimation for ambient backscatter communication systems with massive-antenna reader," *IEEE Trans. Veh. Technol.*, vol. 68, no. 8, pp. 8254–8258, Aug. 2019.

[18] Md. L. Rahman, J. A. Zhang, X. Huang, Y. J. Guo, and R. W. Heath, "Framework for a perceptive mobile network using joint communication and radar sensing," *IEEE Trans. Aerosp. Electron. Syst.*, vol. 56, no. 3, pp. 1926–1941, Jun. 2020.

[19] H. Chu, L. Zheng, and X. Wang, "Super-resolution mmWave channel estimation for generalized spatial modulation systems," *IEEE J. Sel. Topics Signal Process.*, vol. 13, no. 6, pp. 1336–1347, Oct. 2019.

[20] B. Li, X. Zhang, J. Li, and P. Ma, "DOA estimation of non-circular source for large uniform linear array with a single snapshot: Extended DFT method," *IEEE Commun. Lett.*, vol. 25, no. 12, pp. 3843–3847, Dec. 2021.

[21] F. Liu et al., "Integrated sensing and communications: Toward dual-functional wireless networks for 6G and beyond," *IEEE J. Sel. Areas Commun.*, vol. 40, no. 6, pp. 1728–1767, Jun. 2022.

[22] Y. Cui, F. Liu, X. Jing, and J. Mu, "Integrating sensing and communications for ubiquitous IoT: Applications, trends, and challenges," *IEEE Netw.*, vol. 35, no. 5, pp. 158–167, Sep. 2021.

[23] J. A. Zhang et al., "An overview of signal processing techniques for joint communication and radar sensing," *IEEE J. Sel. Topics Signal Process.*, vol. 15, no. 6, pp. 1295–1315, Nov. 2021.

[24] X. Shao, C. You, W. Ma, X. Chen, and R. Zhang, "Target sensing with intelligent reflecting surface: Architecture and performance," *IEEE J. Sel. Areas Commun.*, vol. 40, no. 7, pp. 2070–2084, Jul. 2022.

[25] X. Hu, C. Zhong, Y. Zhang, X. Chen, and Z. Zhang, "Location information aided multiple intelligent reflecting surface systems," *IEEE Trans. Commun.*, vol. 68, no. 12, pp. 7948–7962, Dec. 2020.

[26] Z. Yu, X. Hu, C. Liu, M. Peng, and C. Zhong, "Location sensing and beamforming design for IRS-enabled multi-user ISAC systems," *IEEE Trans. Signal Process.*, vol. 70, pp. 5178–5193, 2022.

[27] X. Tong, Z. Zhang, J. Wang, C. Huang, and M. Debbah, "Joint multi-user communication and sensing exploiting both signal and environment sparsity," *IEEE J. Sel. Topics Signal Process.*, vol. 15, no. 6, pp. 1409–1422, Nov. 2021.

[28] M. Temiz, E. Alsusa, and L. Danoon, "A receiver architecture for dual-functional massive MIMO OFDM RadCom systems," in *Proc. IEEE Int. Conf. Commun. Workshops (ICC Workshops)*, Dublin, Ireland, Jun. 2020, pp. 1–6.

[29] L. Zheng, M. Lops, and X. Wang, "Adaptive interference removal for uncoordinated radar/communication coexistence," *IEEE J. Sel. Topics Signal Process.*, vol. 12, no. 1, pp. 45–60, Feb. 2018.

[30] J. Yuan, Y.-C. Liang, J. Joung, G. Feng, and E. G. Larsson, "Intelligent reflecting surface-assisted cognitive radio system," *IEEE Trans. Commun.*, vol. 69, no. 1, pp. 675–687, Jan. 2021.

[31] H. Zhang, H. Zhang, B. Di, K. Bian, Z. Han, and L. Song, "MetaLocalization: Reconfigurable intelligent surface aided multi-user wireless indoor localization," *IEEE Trans. Wireless Commun.*, vol. 20, no. 12, pp. 7743–7757, Dec. 2021.

[32] F. Zafari, A. Gkelias, and K. K. Leung, "A survey of indoor localization systems and technologies," *IEEE Commun. Surveys Tuts.*, vol. 21, no. 3, pp. 2568–2599, 3rd Quart., 2019.

[33] F. W. Olver, D. W. Lozier, R. F. Boisvert, and C. W. Clark, *NIST Handbook of Mathematical Functions*. New York, NY, USA: Cambridge Univ. Press, 2010.

[34] I. S. Gradshteyn and I. M. Ryzhik, *Table of Integrals, Series, and Products*, 5th ed. New York, NY, USA: Academic, 1994.

[35] S. Hu, F. Rusek, and O. Edfors, "Beyond massive MIMO: The potential of positioning with large intelligent surfaces," *IEEE Trans. Signal Process.*, vol. 66, no. 7, pp. 1761–1774, Apr. 2018.

[36] B. Li, X. Wang, E. Au, and Y. Xin, "Joint localization and environment sensing of rigid body with 5G millimeter wave MIMO," *IEEE Open J. Signal Process.*, vol. 4, pp. 117–131, 2023.

[37] J. Zhu, K. Liu, Z. Wan, L. Dai, T. J. Cui, and H. V. Poor, "Sensing RISs: Enabling dimension-independent CSI acquisition for beamforming," *IEEE Trans. Inf. Theory*, vol. 69, no. 6, pp. 3795–3813, Jun. 2023.

[38] Q. Tao, C. Zhong, H. Lin, and Z. Zhang, "Symbol detection of ambient backscatter systems with Manchester coding," *IEEE Trans. Wireless Commun.*, vol. 17, no. 6, pp. 4028–4038, Jun. 2018.

[39] A. Castaño-Martínez and F. López-Blázquez, "Distribution of a sum of weighted noncentral chi-square variables," *Commun. Stat.*, vol. 34, no. 3, pp. 515–524, Mar. 2005.

[40] A. Papoulis, *Probability, Random Variables, and Stochastic Processes*. New York, NY, USA: McGraw-Hill, 1991.

[41] H. Malik, "Exact distribution of the quotient of independent generalized Gamma variables," *Can. Math. Bull.*, vol. 10, no. 3, pp. 463–465, Nov. 2018.

[42] W. Tang et al., "On channel reciprocity in reconfigurable intelligent surface assisted wireless networks," *IEEE Wireless Commun.*, vol. 28, no. 6, pp. 94–101, Dec. 2021.

Qin Tao received the B.S. degree from the Electronic Information School, Wuhan University, Wuhan, China, in 2017, and the Ph.D. degree in communication and information systems from Zhejiang University, Hangzhou, China, in 2022. She is currently an Associate Professor with the School of Information Science and Technology, Hangzhou Normal University, Hangzhou. Her research interests include backscatter communication, intelligent reflecting surface, symbiotic radio, and orthogonal time frequency space modulation. She and her coauthors received the Best Paper Award at the ICCC 2018, WCSP 2020, and WCSP 2023.

Xiaoling Hu received the B.S. degree in electronics and information engineering from Dalian University of Technology, Dalian, China, in 2016, and the Ph.D. degree in information and communication engineering from Zhejiang University, Hangzhou, China, in 2021. She is currently an Associate Professor with Beijing University of Posts and Telecommunications, Beijing, China. Her research interests include reconfigurable intelligent surface (RIS), integrated sensing and communication (ISAC), wireless sensing, massive MIMO, and mmWave. She was a recipient of the Best Paper Awards at IEEE ICC 2019, IEEE GLOBECOM 2020, IEEE ICC 2022, and WCSP 2023.

Shuowen Zhang received the B.Eng. degree in information engineering from the Chien-Shiung Wu Honors College, Southeast University, Nanjing, China, in June 2013, and the Ph.D. degree from the NUS Graduate School for Integrative Sciences and Engineering (NGS), National University of Singapore, in January 2018, under the NGS Scholarship. From 2017 to 2020, she was a Research Fellow with the Department of Electrical and Computer Engineering, National University of Singapore. Since 2020, she has been with The Hong Kong Polytechnic University, where she is currently an Assistant Professor with the Department of Electrical and Electronic Engineering. Her current research interests include integrated sensing and communication, intelligent reflecting surface-aided communications, unmanned aerial vehicle (UAV) communications, multiuser multiple-input multiple-output (MIMO) communications, communication theory, and optimization methods. She received the Marconi Society Paul Baran Young Scholar Award in 2021, the IEEE Communications Society Young Author Best Paper Award in 2022, the IEEE Communications Society Best Tutorial Paper Award in 2023, and the PolyU Young Innovative Researcher Award in 2023. She served as the Vice Chair for IEEE Communications Society Asia/Pacific Region Board WICE. She served as a Guest Editor for IEEE JOURNAL ON SELECTED AREAS IN COMMUNICATIONS.

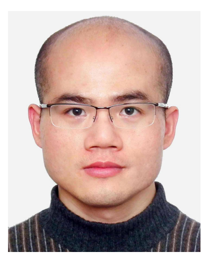

Caijun Zhong (Senior Member, IEEE) received the B.S. degree in information engineering from Xi'an Jiaotong University, Xi'an, China, in 2004, and the M.S. degree in information security and the Ph.D. degree in telecommunications from University College London, London, U.K., in 2006 and 2010, respectively. From September 2009 to September 2011, he was a Research Fellow with the Institute for Electronics, Communications and Information Technologies (ECIT), Queen's University Belfast, Belfast, U.K. Since September 2011, he has been with Zhejiang University, Hangzhou, China, where he is currently a Professor. His current research interests include reconfigurable intelligent surfaces assisted communications and artificial intelligence-based wireless communications. He was a recipient of the 2013 IEEE ComSoc Asia–Pacific Outstanding Young Researcher Award. He and his coauthors received the Best Paper Award at IEEE GLOBECOM 2020 and IEEE ICC 2019. He is an Editor of *Science China Information Sciences* and *China Communications*. He was an Editor of IEEE TRANSACTIONS ON WIRELESS COMMUNICATIONS and IEEE COMMUNICATIONS LETTERS.